Rheology of non-Brownian suspensions of rough frictional particles under shear reversal: A numerical study

François Peters, Giovanni Ghigliotti, Stany Gallier, Frédéric Blanc, Elisabeth Lemaire, Laurent Lobry

Rheology of non-Brownian suspensions of rough frictional particles under shear reversal: a numerical study

François Peters,[1,*] Giovanni Ghigliotti,[2] Stany Gallier,[3] Frédéric Blanc,[1] Elisabeth Lemaire,[1] and Laurent Lobry[1]

[1] *Université Nice Sophia Antipolis - CNRS, Laboratoire de Physique de la Matière Condensée – UMR 7336 Parc Valrose 06100 Nice France*

[2] *Université Joseph Fourier - CNRS Laboratoire des Ecoulements Géophysiques et Industriels - UMR 5519 38400 Saint Martin d'Hères , France*

[3] *SAFRAN-Herakles, Le Bouchet Research Center, 91710 Vert le Petit, France*

(Dated: June 23, 2016)

We perform particle scale simulations of suspensions submitted to shear reversal. The simulations are based on the Force Coupling Method, adapted to account for short range lubrication interactions together with direct contact forces between particles, including surface roughness, contact elasticity and solid friction. After shear reversal, three consecutive steps are identified in the viscosity transient: an instantaneous variation, followed by a rapid contact force relaxation, and finally a long time evolution. The separated contributions of hydrodynamics and contact forces to the viscosity are investigated during the transient, allowing a qualitative understanding of each step. In addition, the influence of the contact law parameters (surface roughness height and friction coefficient) on the transient are evaluated. Concerning the long time transient, the difference between the steady viscosity and minimum viscosity is shown to be proportional to the contact contribution to the steady viscosity, allowing in principle easy determination of the latter in experiments. The short time evolution is studied as well. After the shear reversal, the contact forces vanish over a strain that is very short compared to the typical strain of the long time transient, allowing to define an apparent step between the viscosity before shear reversal and after contact force relaxation. This step is shown to be an increasing function of the friction coefficient between particles. Two regimes are identified as a function of the volume fraction. At low volume fraction, the step is small compared to the steady contact viscosity, in agreement with a particle pair model. As the volume fraction increases, the value of the viscosity step increases faster than the steady contact viscosity, and, depending on the friction coefficient, may approach it.

I. INTRODUCTION

Suspension flows are involved in many industrial processes (fresh concrete handling, food transport, uncured filled polymers) as well as natural or biological flows (blood flow, sediment transport). Much experimental, theoretical and numerical work has been devoted to suspension rheology. Detailed reviews are available in the literature [1–3]. Even non-Brownian suspensions of spherical particles in a Newtonian liquid in creeping flow present striking features: large increase of the viscosity with solid concentration [4], until the suspension finally jams, development of anistropic normal stresses [5–9], shear-induced particle migration [10], mechanical irreversibility [11]. Most of the mentioned properties are connected to the development of a shear-induced microstructure in the suspension, i.e. a particular statistical arrangement of the particle positions. At moderate solid volume fraction, this microstructure is conveniently measured by the pair distribution function, with a high probability of nearly-touching particle pairs in the compressional quadrant of the ambient shear-flow, and a significant concentration depletion in the extensional quadrant [12–18]. For a non-Brownian suspension submitted to creeping flow, such a fore-aft asymmetric microstructure can develop only if the particles exert non-hydrodynamic forces on each other [19]. In the case of large hard particles, if the experimental pair distribution function has revealed that direct contact between particles, promoted by the surface asperities, has to be considered [12, 15], the question of the exact nature of the contact forces is still a largely open question. In some recent simulations concerning suspensions of frictional particles [18, 20], a large influence of friction on the rheological properties has been evidenced. In particular, the computed suspension viscosity is greatly enhanced, up to experimental values [18]. This increase originates mostly in the growth of the direct contact force contribution while the hydrodynamic contribution hardly changes. For smaller particles, where colloidal forces are relevant too, friction has been proposed to explain discontinuous shear-thickening of suspensions [21–23]: as the shear rate is increased, the contact switches from lubricated to frictional, inducing a sharp increase of the viscosity. More generally, microstructure and contact forces act together to produce enhanced stresses in the suspension: the shear flow brings the particles closer to each other, mostly in the compressional direction of the flow, thus promoting contact between particles, which induces large stresses [18].

In bulk rheology, the shear-induced microstructure has

* peters@unice.fr

been first revealed in shear reversal experiments [24–27]. In such experiments, the suspension is first sheared in a steady way. As the shear rate is reversed, a transient occurs, where the viscosity undergoes a step-like decrease, goes to a minimum and increases again to its steady value (see Fig. 1 for an experimental transient from [27]). In

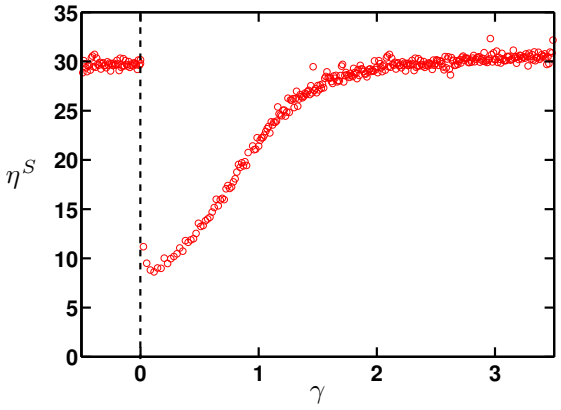

FIG. 1. Experimental relative viscosity η^S transient as a function of shear strain γ from [27]. PMMA particles, 30 μm in diameter, in a Newtonian liquid. Solid volume fraction $\phi = 0.444$.

the case of non-Brownian suspensions, this transient does not depend on the shear rate, except for a slight shear-thinning behavior [24, 27], and the viscosity only depends on the total strain after shear reversal. Normal stress difference measurements exhibit similar transients [25, 26]. The origin of such transients is now qualitatively understood: due to fore-aft asymmetry, the steady microstructures after and before shear reversal are different, and the necessary reorganization of the particles results in the observed rheological transient. From a more quantitative point of view, Blanc et al. [27] pointed out that the steady viscosity and minimum viscosity do not depend on the volume fraction in the same way. In particular, the measured minimum viscosity is quite close to the viscosity of simulated random suspensions, i.e. suspensions where the particles are randomly placed at each step of the computation (while taking care that they do not overlap) and that do not present shear-induced microstructure [28]. It suggests that, as the viscosity goes to its minimum value, the initial shear-induced microstructure is broken. The following viscosity increase is produced by the re-building of the microstructure. As a consequence, the difference between steady and minimum viscosity can be seen as the viscosity increment due to the shear-induced microstructure. As the solid concentration goes to the jamming volume fraction, this increment becomes increasingly predominant, and the minimum viscosity becomes very small compared to the steady viscosity.

However, a precise understanding of the transient is still missing. Few numerical studies are available in the literature on this subject. Bricker and Butler [29] performed simulations of a particle monolayer in Stokesian dynamics. The particles exert on each other double layer-like forces along the line of particle centers, without friction force. These simulations are in qualitative agreement with experiments: the viscosity goes to a minimum, that is deeper for denser suspensions, and the transient occurs over a typical strain that decreases as the solid volume fraction increases. However, they do not evidence any viscosity step at shear reversal. The first normal stress difference N_1 was computed too. At shear reversal, N_1 instantaneously changes sign, then vanishes and finally reaches the value it had before shear reversal. Bricker & Butler could relate the rheological transient to the evolution of the microstructure. In particular, the viscosity minimum happens when the pair distribution function is approximately fore-aft symmetric, with much less particles near contact. Another set of simulations was performed by Stickel et al. [30] using the accelerated Stokesian dynamics, where the particles exert the same type of force on each other as in [29]. In this paper, the suspensions are submitted to step variations of the shear rate, either start-up flow, shear rate increase or decrease and shear reversal. The main purpose of the paper was to compare the output of a previously published constitutive model [31] for structure and total stress in suspensions to the simulation results, as well as to experimental data. Only one solid volume fraction and one parameter set for the interparticle force is considered. However, the same qualitative trends as in experiments were noted, and some qualitative explanation were given, using a structure tensor computed from the simulations. In addition, an article with a quite similar scope was published recently [32]. Both papers share some qualitative conclusions, as mentioned in different part of the present article.

Finally, it should be noted that a lot of work has been devoted to the response of suspensions to oscillatory shear flow [24, 33–37]. Some exciting properties were evidenced: the viscosity strongly depends on strain amplitude, suggesting the development of a particular microstructure that evolves with strain amplitude and the time that is necessary for this microstructure to re-build depends on the strain amplitude [36, 37], presumably due to self-organization of the particles [11, 38]. Such an irreversible evolution has been also evidenced for a sheared suspension drop in an otherwise pure liquid [39]. In addition, superposition of oscillatory and steady cross-shear flows results in complex rheological response [40, 41]. As in the case of shear reversal, the response is driven by the time evolution of the microstructure under the simultaneous action of interacting forces and hydrodynamic interactions. However, a quantitative relation between both types of time-dependent response is not easy to extract.

In the present paper, we report simulations of shear reversal in non-Brownian suspensions of rough frictional particles. Since simulations provide insight into quantities that are not available in experiments, such as in-

terparticle forces, separate measurement of contact and hydrodynamic contribution to the stress, instantaneous stress variations, we seek a deeper understanding of all steps of the transient. In particular, the question is addressed whether quantitative information can be extracted from the transient, concerning either bulk quantities or particle-scale properties like surface roughness height and friction. The numerical method, including the contact force model, is first explained in section II. The results are presented in Sec. III, including a general description of a typical transient (Sec. III A), followed by some features of the response to steady shear (Sec. III B). The long time transient is then investigated (Sec. III C), while the short time evolution is deferred to Sec. III D. We have chosen to focus on the shear stress response. While normal stress differences are of interest, in particular in time-dependent flows, a proper treatment of both shear and normal stress may have been, in our opinion, at the expense of clarity. A lot of features that are evidenced while investigating shear stress qualitatively apply to normal stress differences as well.

II. NUMERICAL METHOD

A. The Force Coupling Method

In the present study we use the Force Coupling Method (FCM) to study numerically the dynamics of a suspension of non-Brownian rigid spherical particles. FCM was introduced by Maxey and collaborators [42–44], and we follow the approach developed by Yeo and Maxey [45, 46]. The reader is referred to Ref. [47] for a detailed presentation of the method and computations, and we give here only a brief overview.

In FCM, the equation for the motion of the fluid is solved in the whole spatial domain, i.e. in the volume occupied by the fluid and by the particles, whose presence is modeled through a force density field acting on the fluid. Also, zero mean deformation is imposed within the volume occupied by each particle.

In the limit of vanishing inertia (zero Reynolds number) the fluid motion obeys the Stokes equations

$$\begin{aligned} -\boldsymbol{\nabla} p + \eta \nabla^2 \mathbf{u} + \mathbf{f} &= 0 \\ \nabla \cdot \mathbf{u} &= 0 \end{aligned} \tag{1}$$

where p and $\mathbf{u}$ are the fluid pressure and velocity fields, η is the fluid viscosity and $\mathbf{f}$ represents the volume force density acting on the fluid. The force density representing the particles is

$$f_i = \sum_{n=1}^{N_p} \left\{ F_i^n \Delta_M(\mathbf{x} - \mathbf{X}^n) + G_{ij}^n \frac{\partial}{\partial x_j} \Delta_D(\mathbf{x} - \mathbf{X}^n) \right\} \tag{2}$$

where $\mathbf{X}^n$ is the location of the center of mass of the n^{th} particle, F_i the force monopole induced by the particle and G_{ij} the corresponding force dipole and N_p is the number of particles in the suspension. F_i and G_{ij} come from a multipolar development of the perturbation of the particle to the flow, and represent the dominant far-field contributions. Δ_M and Δ_D are the FCM force envelopes, standing for the extent of each particle, and are given by:

$$\begin{aligned} \Delta_M(\mathbf{x}) &= \tfrac{1}{(2\pi\sigma_M^2)^{3/2}} e^{-\frac{\mathbf{x}^2}{2\sigma_M^2}} \\ \Delta_D(\mathbf{x}) &= \tfrac{1}{(2\pi\sigma_D^2)^{3/2}} e^{-\frac{\mathbf{x}^2}{2\sigma_D^2}} \end{aligned} \tag{3}$$

where $\sigma_M = \frac{a}{\sqrt{\pi}}$ and $\sigma_D = \frac{a}{(6\sqrt{\pi})^{1/3}}$ are the envelope length scales and a is the particle radius. The force monopole $\mathbf{F}$ is the force exerted by a particle on the fluid, while the force dipole is linked both to the torque exerted by the fluid on the particle and to the rigidity constraint within the volume occupied by the particle. The antisymmetric part of the force dipole moment, T_{ij} is connected to the hydrodynamic torque $\mathbf{T}^h$ on the particle using the Levi-Civita symbol ϵ_{ijk} according to

$$T_{ij} = -\frac{1}{2} \epsilon_{ijk} T_k^h \tag{4}$$

while the symmetric part S_{ij} is the so-called hydrodynamic stresslet exerted by the fluid on the particle. It is determined from the constraint of zero net deformation within the particle, that reads

$$\int e_{ij} \Delta_D(\mathbf{x} - \mathbf{X}^n) d\mathbf{x} = 0 \tag{5}$$

where $e_{ij} = \frac{1}{2}(\frac{\partial u_i}{\partial x_j} + \frac{\partial u_j}{\partial x_i})$ denotes the strain rate.

The particle motion obeys Newton's equations. The particle inertia is neglected, so that the monopole moment and the hydrodynamic part of the dipole moment are determined from the external force and torque on the particles

$$\begin{aligned} \mathbf{F}^h + \mathbf{F}^e &= -\mathbf{F} + \mathbf{F}^e = 0 \\ \mathbf{T}^h + \mathbf{T}^e &= 0 \end{aligned} \tag{6}$$

where the superscripts h and e stand for hydrodynamic and external respectively. In the present article, $\boldsymbol{F^e}$ and $\boldsymbol{T^e}$ originate in the interactions between particles (see paragraph II C).

The linear and angular velocities of each particle are defined as follows

$$\begin{aligned} \mathbf{U}^n &= \textstyle\int \mathbf{u}(\mathbf{x}) \Delta_M(\mathbf{x} - \mathbf{X}^n) d\mathbf{x} \\ \boldsymbol{\Omega}_i^n &= \tfrac{1}{2} \textstyle\int \epsilon_{ijk} \frac{\partial u_k}{\partial x_j} \Delta_D(\mathbf{x} - \mathbf{X}^n) d\mathbf{x} \end{aligned} \tag{7}$$

In conclusion, FCM is solving the fluid motion equation, in which a force term is introduced to represent the particles, Eqs. (1)-(2) together with Eqs. (4)-(6). The knowledge of the imposed flow, the external forces and the constraint of zero mean deformation within the particle volumes allow to determine the stresslet coefficients and thus the velocity field in the presence of the particles. Finally, this allows to compute the particle dynamics.

B. The lubrication correction

The original FCM is only a long range approximation. However, depending on the direct interaction force, particles can be as close as $10^{-3}a$ to each other. For such neighboring particles, the FCM strongly underestimates the hydrodynamic interactions. To include the short range lubrication force, we proceed as in Ref. [46, 47].

The FCM is formally equivalent to solving a mobility problem in the form

$$\begin{bmatrix} \boldsymbol{\mathcal{U}} - \boldsymbol{\mathcal{U}}^{\infty} \\ \mathbf{E}^{\infty} \end{bmatrix} = \mathbf{M}^{FCM} \begin{bmatrix} \boldsymbol{\mathcal{F}} \\ \mathbf{S} \end{bmatrix} \tag{8}$$

where $\boldsymbol{\mathcal{U}}$ is a $6N_p$-dimensional array containing the linear and angular particle velocities, $\boldsymbol{\mathcal{F}}$ is a $6N_p$-dimensional array containing the particle monopole coefficients and the torques. $\boldsymbol{\mathcal{U}}^{\infty}$ is the $6N_p$-dimensional array containing the linear and angular velocities of the imposed flow calculated at the particle centers. $\mathbf{S}$ is a $5N_p$-dimensional array containing the five independent stresslet coefficients for each particle (the stresslet is symmetric and only the traceless part is considered here), and $\mathbf{E}^{\infty}$ is a $5N_p$-dimensional array containing the corresponding strain rate of the imposed velocity field. M^{FCM} is called the grand mobility matrix and represents the linear relationship existing in a creeping flow between these quantities. Since $\boldsymbol{\mathcal{F}}$ and $\mathbf{S}$ contain far-field contributions of particle-particle hydrodynamic interactions, $\mathbf{M}^{FCM}$ represents a far-field approximation of the exact grand mobility matrix. The unknowns in this system are $\boldsymbol{\mathcal{U}}$ and $\mathbf{S}$. It should be stressed that the elements of the matrix M^{FCM} are never computed, rather a fluid solver is used to compute the velocity field given a certain force distribution.

In order to include the effect of short-range lubrication forces, the mobility problem (8) is formulated as a resistance problem:

$$\begin{bmatrix} \boldsymbol{\mathcal{F}} \\ \mathbf{S} \end{bmatrix} = \left(\mathbf{M}^{FCM}\right)^{-1} \begin{bmatrix} \boldsymbol{\mathcal{U}} - \boldsymbol{\mathcal{U}}^{\infty} \\ \mathbf{E}^{\infty} \end{bmatrix} \tag{9}$$

where $\left(\mathbf{M}^{FCM}\right)^{-1}$ is a far-field approximation of the resistance matrix, and then adding a resistance matrix $\mathbf{L}$ containing the lubrication correction [45, 46, 48, 49]:

$$\begin{bmatrix} \boldsymbol{\mathcal{F}} \\ \mathbf{S} \end{bmatrix} = \left(\left(\mathbf{M}^{FCM}\right)^{-1} + \mathbf{L}\right) \begin{bmatrix} \boldsymbol{\mathcal{U}} - \boldsymbol{\mathcal{U}}^{\infty} \\ \mathbf{E}^{\infty} \end{bmatrix} \tag{10}$$

where $\boldsymbol{\mathcal{F}}$ and $\mathbf{S}$ now contain both the long range and lubrication interactions. More precisely, since a part of the close interaction is already taken into account in the original FCM, $\mathbf{L}$ contains the difference between the exact resistance matrix $\mathbf{L}^{2B}$ from the two-body problem and the corresponding far-field resistance matrix $\left(\mathbf{M}^{FCM}\right)^{-1}$: $\mathbf{L} = \mathbf{L}^{2B} - \mathbf{L}^{FCM}$. The coefficients of the matrix $\mathbf{L}^{FCM}$ are determined once and for all and are expressed as polynomial functions of the inter-particle separation. In calculating the lubrication correction, we have found negligible differences with the FCM resistance functions tabulated in Ref. [46]. Finally, the system in Eq. (10) is solved for $\mathbf{S}$ and $\boldsymbol{\mathcal{U}}$ following a procedure detailed in Refs. [45, 46].

C. The contact forces between particles

In addition to the hydrodynamic forces (far-field and lubrication contributions) described above, we include the possibility for the particles to have solid (direct) contacts with each other. We consider the spherical particles, of radius a, to have sparse surface roughness, of characteristic height h_r. Under these conditions, we can assume that contact appears if the distance between two particle surfaces $\delta = (r - 2a)$ becomes smaller than h_r, where $r = ||\mathbf{r}|| = ||\mathbf{X}^2 - \mathbf{X}^1||$ is the distance between the particle centers. It is worth noting that even in the presence of a solid contact we suppose that the lubrication forces do not vanish, since the two mean particle surfaces are still at a nonzero distance. For this reason, the lubrication forces are not switched off for $\delta \leq h_r$. In our model, we account both for normal and tangential (frictional) contact forces.

We model the solid contact in the direction normal to the particle surfaces using the Hertz law, that we apply between an asperity of one particle and a smooth patch of the surface of another particle:

$$\mathbf{F}_n^c = -\kappa_n (h_r - \delta)^{\frac{3}{2}} \mathbf{n} \tag{11}$$

where $\mathbf{n} = \mathbf{r}/||\mathbf{r}||$ and

$$\kappa_n = \frac{4}{3} \frac{E}{2(1-\nu^2)} h_r^{\frac{1}{2}} \tag{12}$$

E being the Young modulus and ν the Poisson ratio [50, 51]. In a dilute suspension submitted to a shear rate $\dot{\gamma}$, the typical hydrodynamic force between two particles in contact is $6\pi\eta\dot{\gamma}a^2$ [52]. Then, the relative importance of contact with respect to hydrodynamic forces is expressed by the dimensionless parameter

$$\dot{\Gamma} = \frac{6\pi\eta\dot{\gamma}a^2}{F_0} \tag{13}$$

where $F_0 = \kappa_n h_r^{3/2}$ is the magnitude of the force needed

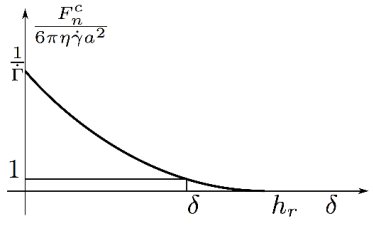

FIG. 2. Normalized contact force as a function of surface-to-surface distance δ. $\bar{\delta}$ is the typical surface-to-surface distance.

for the complete deformation of the asperity, as shown

in Fig. 2 where the normalized normal contact force is displayed. The typical distance between particle surfaces $\bar{\delta}$ is determined by equating the hydrodynamic and contact forces (Fig. 2), yielding for the typical roughness deformation $\bar{\epsilon}$:

$$\bar{\epsilon} = (h_r - \bar{\delta})/h_r = \dot{\Gamma}^{2/3} \tag{14}$$

The frictional force is modeled as a spring-like force with a threshold:

$$\mathbf{F}_t^c = \begin{cases} -\kappa_t \mathcal{Y} & \text{for} \quad F_t^c < \mu F_n^c \\ \mu F_n^c \frac{\mathbf{F}_t^c}{F_t^c} & \text{otherwise} \end{cases} \tag{15}$$

with μ the (dynamic) friction coefficient. In our model, we assume the static friction coefficient to have the same value of the dynamic one. $\mathcal{Y}$ is the relative tangential displacement of the two particle surfaces and it is calculated as the integral of the slip velocity during contact:

$$\mathcal{Y} = \int_0^t \mathbf{U}^s dt \tag{16}$$

and the slip velocity between particles i and j is computed as

$$\mathbf{U}^s = \mathbf{U}_i - \mathbf{U}_j - [(\mathbf{U}_i - \mathbf{U}_j)\cdot\mathbf{n}]\,\mathbf{n} + (a\mathbf{\Omega}_i + a\mathbf{\Omega}_j)\times\mathbf{n} \tag{17}$$

When slip occurs (second line in Eq. 15), the force is incremented as in the stick phase, and its intensity is then rescaled to obey the dynamic friction law. As a consequence, there cannot be any discontinuity in the time evolution of the contact forces. In addition, only the direction of the relative tangential displacement $\mathcal{Y}$ changes in the slip-phase while its length is kept constant. The value of the stiffness of the tangential spring, κ_t, is linked to the normal stiffness κ_n through [53, 54]

$$\kappa_t = \frac{2}{7}\kappa_n \sqrt{\delta} \tag{18}$$

The contact force between particles introduces a torque on each particle given by

$$\mathbf{T}^c = a\mathbf{n} \times \mathbf{F}_t^c \tag{19}$$

since the normal component of the contact force $\mathbf{F}_n^c$ does not contribute to the torque.

The contact force contributes to the total stresslet of the system, with a term

$$\mathbf{S}^c = \frac{1}{2}\left(\mathbf{F}^c \otimes \frac{\mathbf{r}}{2} + \frac{\mathbf{r}}{2} \otimes \mathbf{F}^c\right) \tag{20}$$

for each of the two particles involved in the contact.

D. Solution procedure

The numerical solution of FCM proceeds as follows. Contact forces acting on the particles are computed from the positions and integrated relative slip velocities of the particles obtained at the previous time step. A conjugate gradient method is used to solve equation (10) iteratively, where M^{FCM} represents the Stokes solver, implemented through a spectral method (Fast Fourier Transform) owing to the triple periodicity of the computational domain. Following Yeo [47], the computational domain is treated using Lees-Edwards periodic boundary conditions. Once the velocity field is obtained, particle velocities are computed with (7) and (7). A second-order Adams-Bashforth scheme is finally used to update the particle positions at the following time step. Our computational domain is a cubic box meshed with 64^3 gridpoints, corresponding to 32 particle radii in each direction. Depending on volume fraction, the number of particles in the cell ranges from 1565 to 3911. The effect of the cell size was not extensively studied. For a typical suspension $\phi = 0.45$, $h_r/a = 5.10^{-3}, \mu = 0.5$, the size of the cubic cell was divided by 2 (16 particle radii in each direction) with no effect on the transient, except for the larger statistical fluctuations. In units of $\dot{\gamma}^{-1}$, the time step is taken to be $5 \cdot 10^{-4}$ unless otherwise specified. Computing times range from less than a day to a few weeks on two cores of a 2.6 GHz CPU, depending mostly on particle concentration $\phi = \frac{4N_p}{3V}\pi a^3$, roughness height h_r and friction coefficient μ.

E. Definition of the rheological quantities

The bulk stress of a suspension of particles is defined as [55]:

$$\Sigma_{ij} = -p\delta_{ij} + 2\eta E_{ij}^{\infty} + \Sigma_{ij}^p \tag{21}$$

where Σ_{ij}^p is the particle contribution to the bulk stress. It has both hydrodynamic and contact contributions, $\Sigma_{ij}^p = \Sigma_{ij}^H + \Sigma_{ij}^C$, which are function of the particle stresslet:

$$\begin{aligned} \Sigma_{ij}^H &= \frac{1}{V}\sum_{n=1}^{N_p} \mathbf{S}_{ij}^n \\ \Sigma_{ij}^C &= \frac{1}{V}\sum_{n=1}^{N_p} \mathbf{S}_{ij}^{C,n} \end{aligned} \tag{22}$$

We have used the notations $\mathbf{S}_{ij}^n$ and $\mathbf{S}_{ij}^{C,n}$ to denote the hydrodynamic particle stresslet (Eq. (10)) and the contact particle stresslet, from Eq.(20).

In the present study, we consider a particle suspension subject to an imposed linear shear flow

$$\mathbf{u}^{\infty} = \dot{\gamma} y \mathbf{e}_x \tag{23}$$

so that $\mathbf{e}_x$ is along the velocity direction, $\mathbf{e}_y$ along the velocity gradient and $\mathbf{e}_z$ along the vorticity. The relative viscosity η^S can be split into the hydrodynamic η^H and

contact contributions η^C:

$$\begin{aligned}\eta^S &= \left(1+\frac{\Sigma^p_{xy}}{\eta\dot\gamma}\right)\\ &= \left(1+\frac{\Sigma^H_{xy}}{\eta\dot\gamma}\right)+\frac{\Sigma^C_{xy}}{\eta\dot\gamma}\\ &= \eta^H+\eta^C\end{aligned} \tag{24}$$

These rheological quantities will be extensively analyzed and discussed in the following section.

We note here that the torque exerted by friction forces on the particles is balanced by the hydrodynamic torque due to the lack of particle inertia, leading to symmetric stress tensor. In addition, it turns out that the frictional torque keeps very small compared to the stresses in all stages of the transient (the antisymmetrice contact stress is at most 2% of its symmetric counterpart). As a consequence, it is not further studied.

Finally, we stress that the contact contribution as defined in Eq. 24 is the direct contribution of the contact force from the contact stresslet (Eq. 20), with no hydrodynamic contribution. A different splitting, which takes advantage of the linearity of Stokes equation, is proposed in Sec. III D 2.

F. Choice of parameter values

In this section we discuss the values of the parameters used in the numerical model. In order to be able to compare our results to existing and possible future experiments, we consider here typical experimental values. Several experiments have been carried out in the past on suspensions of polystyrene or PMMA (Poly-methylmetacrylate) beads [24–27] characterized by a Young modulus $1.8 \lesssim E \lesssim 3GPa$ and a Poisson ration $\nu \simeq 0.4$. The typical flow and geometrical parameters found in such experiments are given in Table I, together with the corresponding values of the dimensionless parameters. The physical parameters that define the modeled sheared suspension are reduced to several dimensionless parameters, namely ϕ, h_r/a, μ and $\dot\Gamma$ (or equivalently $\bar\epsilon$), together with the dimensionless time $\dot\gamma t$. One of the goals of this paper is to understand what influence those dimensionless parameters have on the observed viscosity transient. It should be noted that the values of the dimensionless hydrodynamic force $\dot\Gamma$ computed for usual non-Brownian suspensions (Table I) keeps small compared to 1. In such a case, it turns out that $\dot\Gamma$ has a very weak influence on the steady rheological properties [18]. To be more specific, this model yields a very weak shear-thickening behavior. In addition, the main expected effect of this parameter on the transient would be to change the contact force relaxation time τ_s. It will be shown later (Sec. III D 1) that $\dot\gamma\tau_s$ is directly connected to the typical compression of the surface asperities $\bar\epsilon$, and thus is expected to keep quite small compared to the other typical strain of the transient (Sec. III C). For those reasons, and also in order to keep the time step approximately constant in the different simulations, $\dot\Gamma$ will be set to the quite small value 10^{-2} throughout this study, so that $\bar\epsilon \approx 4.6\ 10^{-2}$. Let us recall that $\bar\epsilon$ corresponds to the typical asperity deformation in the idealized case of a collision between two particles in an otherwise pure liquid. In the actual simulations where $0.2 \le \phi \le 0.5$, the value of the average asperity deformation is bigger. For example, with $\phi = 0.5$, $\mu = 0.3$ and $h_r/a = 5.10^{-3}$ the most probable compression is 0.2, with a quite large distribution. The simulations are restricted to volume fraction lower than 0.5 in order to avoid crystallization of our monodisperse suspension. Finally, the value of h_r/a is varied in the range $5.10^{-3} \le h_r/a \le 2.10^{-2}$.

III. RESULTS

A. A typical shear reversal simulation

For each value of the parameters ϕ, h_r, μ, the suspension is submitted to the velocity field $\mathbf{u}^\infty(t<0) = \dot\gamma y \mathbf{e}_x$ for a deformation of $\dot\gamma t$=10 to insure steady rheological properties. At time $t = 0$ the shear rate is suddenly inverted: $\mathbf{u}^\infty(t>0) = -\dot\gamma y \mathbf{e}_x$. The data are averaged over eight simulations that were started from eight independent initial conditions, but for otherwise identical parameters. The initial conditions are sampled from the steady state of a constant shear simulation. Sampling occurs at strain separations of more than two, in order to ensure uncorrelated particle positions.

Before engaging into a detailed parametric study, we show the variation with time of the relative viscosity in a typical numerical simulation. We consider a suspension with $\phi = 0.45$, $\mu = 0.5$, $h_r/a = 5.10^{-3}$. Fig. 3 reports the measured viscosity as a function of total strain from shear reversal together with its components from Eq. (24), coming from hydrodynamic interactions η^H and contact forces η^C. At $t = 0$ shear reversal takes place. We observe an instantaneous drop of the relative viscosity from $\eta^S_{(0^-)}$ to $\eta^S_{(0^+)}$ (Fig. 3 and 4), that will be discussed in detail in section III D 2. Here we simply mention that this drop is due to the action of the unchanged contact forces (Eq. (20)), that switches from resistive to propulsive in the reversed flow, so that the contact contribution changes sign, while lubrication forces instantaneously grow to higher values and oppose the separation of neighboring particles (see also Sec. III D and Fig. 9). Shortly thereafter, the majority of contacts between particles disappear, due to the separation of nearest neighboring particles. This happens in a characteristic strain $\dot\gamma\tau_s$ determined by the relaxation of contact forces. $\dot\gamma\tau_s$ depends on the chosen contact model, and in particular on the value of the normal stiffness κ_n. Its determination is discussed in paragraph III D 1. The viscosity after force relaxation is extrapolated to $\dot\gamma t = 0$, giving η^S_{init} (Fig. 4).

Physical parameters				Dimensionless parameters	
η_0	$\dot{\gamma}$	h_r/a	μ	$\dot{\Gamma}$	$\bar{\epsilon}$
1 $Pa.s$	10^{-2} - 10 s^{-1}	10^{-3} - 10^{-1}	0 - 1	10^{-8} - 10^{-1}	$5 \cdot 10^{-6}$ - 0.2

TABLE I. Values of the physical parameters (suspending fluid viscosity η_0, shear rate $\dot{\gamma}$, dimensionless particle roughness h_r/a and friction coefficient μ) and corresponding values of $\dot{\Gamma}$ (Eqs. (12) and (13)) and $\bar{\epsilon} = \dot{\Gamma}^{2/3}$.

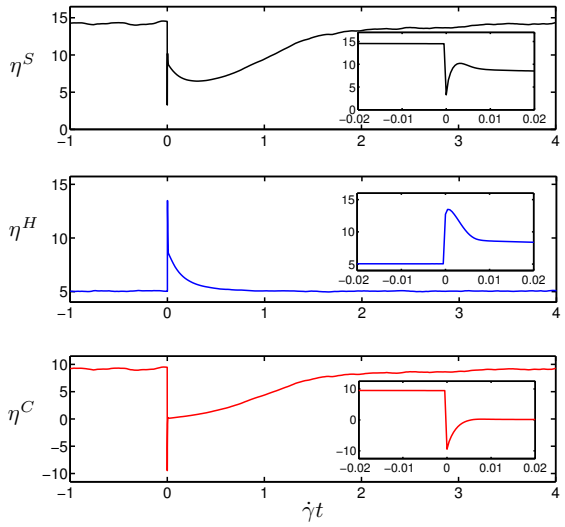

FIG. 3. The relative viscosity η^S of a suspension under shear reversal $\phi = 0.45$, $\mu = 0.5$, $h_r/a = 5.10^{-3}$ as a function of shear strain $\dot{\gamma}t$ (top), together with the hydrodynamic contribution η^H (middle) and contact contribution η^C (bottom) from Eq. (24). The inset shows the fast dynamics due to the relaxation of the contact forces. The shear reversal takes place at $t = 0$.

On a longer time scale, the suspension viscosity goes through a minimum η^S_{min} at the strain γ_{min}, that is determined by the decrease of lubrication forces (nearest neighboring particles separate more and more from each other) and the increase of the contact forces. The latter is due to the development of new contacts following the restructuration of the suspension in the reversed flow. Gradually, the suspension microstructure reforms: the contact forces drive the climb of the relative viscosity back to the pre-shear value.

The tangential and normal contact force contributions to the viscosity are not separated in Fig. 3. Actually, the tangential force contribution roughly follows the qualitative behavior of the normal force contribution while keeping smaller. This will be briefly shown in Sec. III D. Nevertheless, friction plays a major role in suspension rheology, and in particular greatly increases the magnitude of the normal contact forces, as will be shown in section III B.

In addition, the solver and lubrication correction (Eq. (10)) are not separated either in Fig. 3, since our lubrication stress is only a correction, i.e. corresponds to the flow that the solver cannot resolve, and also for the sake of figure clarity. However, we note here that most of the hydrodynamic variations are due to lubrication corrections.

Before detailing the evolution of the system at longer times in Sec. III C, we discuss the influence of friction and roughness on the steady viscosity in Sec. III B. The dynamics immediately after shear reversal $0 \leq t \leq \tau_s$ is deferred to Sec. III D.

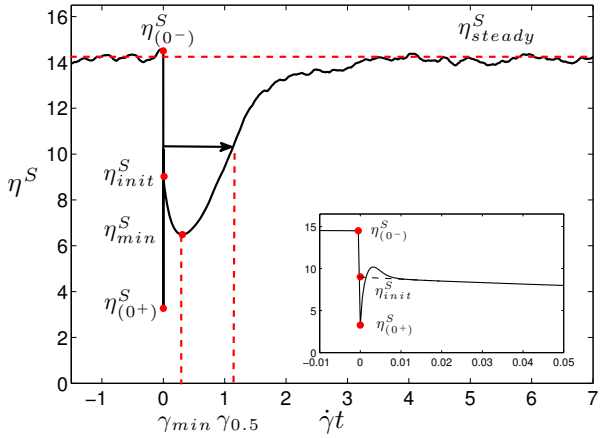

FIG. 4. Definition of the quantities of interest for the transient after shear-reversal of the shear viscosity η^S as a function of shear strain $\dot{\gamma}t$.

B. Steady shear

In this section, the influence of the friction coefficient and roughness height on the steady viscosity is addressed. η^S_{steady} is computed as the average of the viscosity over the strain interval $-5 \leq \dot{\gamma}t \leq 0$, i.e. in the steady shear before shear reversal. As displayed in Fig. 5, friction between particles induces a large increase of the suspension steady viscosity. The hydrodynamic part is not altered, while the contact contribution can be enhanced by up to a factor of 5 at ϕ=0.5. We note that this is not the result of the single addition of the interparticle tangential force contribution to the viscosity computed without friction, since the former amounts to at most 25% of the contact viscosity in the present volume fraction range (Fig. 18). The normal component of the force is still responsible

for the main part of the contact viscosity, and is largely enhanced by friction.

The lack of hydrodynamic contribution variation with

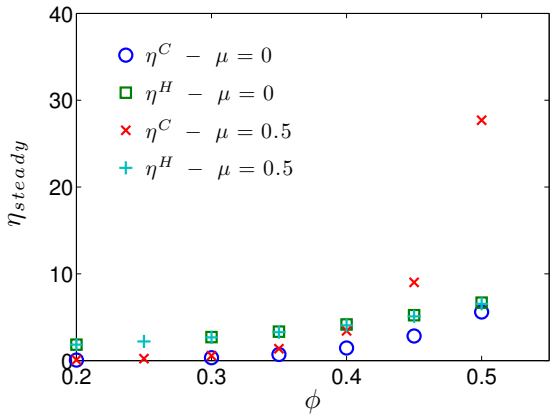

FIG. 5. Contact and hydrodynamic contributions to the steady viscosity as a function of solid volume fraction ϕ, without and with friction between particles. Roughness height h_r/a=5. 10^{-3}.

friction is a little surprising, since all contributions are related to the particles arrangement and motion. This has already been evidenced by Gallier et al. [18], where it has been shown in addition that for moderate volume fraction $\phi \leq$0.4, the hydrodynamic viscosity or a sheared suspension is very close to the viscosity computed for random suspensions, for which no shear-induced microstructure develops. The fact that such different microstructures produce the same hydrodynamic viscosity will be examined in section III C.

The surface roughness height has weaker influence on the viscosity, at least in the range of interest in the present work $5.10^{-3} \leq h_r/a \leq 2.10^{-2}$ and $0.2 \leq \phi \leq 0.5$, as shown in Fig.6. More precisely, as h_r/a is increased, the hydrodynamic contribution decreases, probably due to the decrease of the lubrication interactions, while the contact contribution increases or decreases, depending on the friction coefficient μ and on the solid volume fraction. The variations of both contributions are moderate.

The variation of the computed suspension viscosity with volume fraction is well approximated by the classical Maron-Pierce Law [56]:

$$\eta^S \propto (\phi^* - \phi)^{-2} \tag{25}$$

as shown in Fig. 7(a). Again, unlike the friction coefficient, the roughness height has little effect on the suspension viscosity, and particularly on the jamming solid volume fraction ϕ^* that can be deduced from the fit of the computed viscosity to Maron-Pierce law. Figure 7(b) displays the evaluated jamming solid volume fraction as a function of friction coefficient μ for different values of the roughness height h_r/a. ϕ^* significantly decreases from

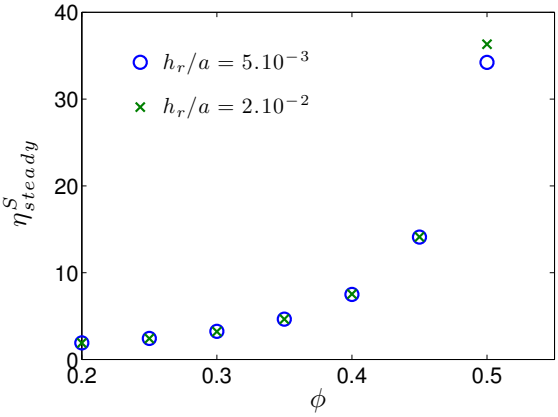

FIG. 6. Steady suspension viscosity as a function of solid volume fraction for different values of the roughness height h_r/a. Friction coefficient $\mu = 0.5$.

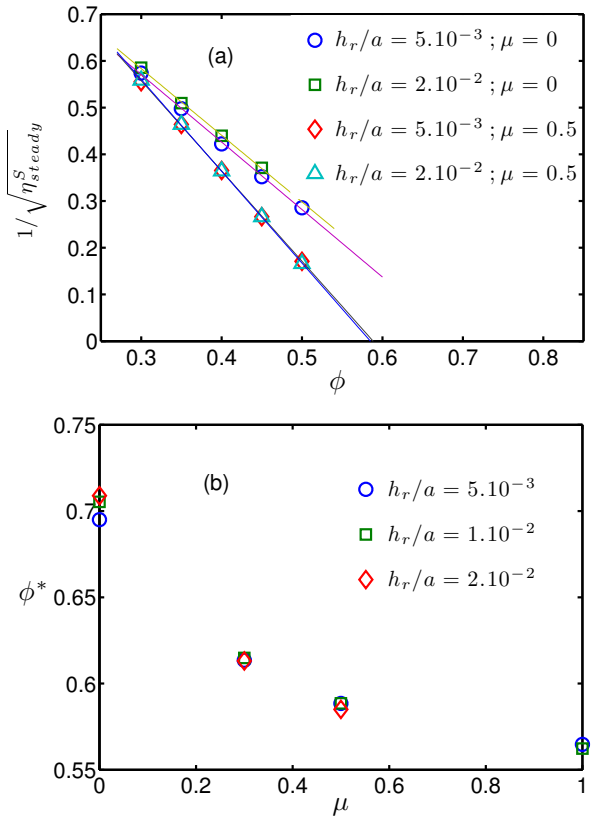

FIG. 7. (a) Determination of the scaling law for the viscosity as a function of volume fraction ϕ. Symbol: computation. Solid line: fit to Maron-Pierce law Eq. (25). (b) Jamming volume fraction ϕ^* as a function of friction coefficient μ for different values of the roughness height h_r/a.

approximately 0.7 to 0.56 as the friction coefficient is increased from 0 to 1. Such variations have already been

evidenced in simulations concerning discontinuous shear-thickening suspensions [22]. In the friction regime, the jamming volume fraction was shown to decrease from 0.66 to 0.58 for the same range of friction coefficient. Both studies are thus in qualitative agreement, and the discrepancies may be explained by the probed volume fraction range: in the present paper, the volume fraction is kept below 0.5, while Mari et al. consider values closer to the jamming volume fraction. We note that the experimental values of the jamming volume fraction from the literature span a quite wide range too [3, 4, 27, 57].

C. Long time transient

This section is devoted to the dynamics of the suspension after the contact forces have relaxed $\dot{\gamma}t \gtrsim \dot{\gamma}\tau_s$. We recall the quantities of interest in this part of the transient. As shown in Fig. 4, η^S_{init} is the viscosity after contact force relaxation extrapolated to time t=0. At strain γ_{min} the suspension viscosity takes its smallest value η^S_{min}. At the end of the transient, the viscosity reaches its steady value η^S_{steady}. The strain $\gamma_{0.5}$ leading from η^S_{min} to 50% of the relaxation to the steady value is defined as:

$$\eta^S(\gamma_{0.5}) \equiv \eta^S_{min} + 0.5\ (\eta^S_{steady} - \eta^S_{min}) \qquad (26)$$

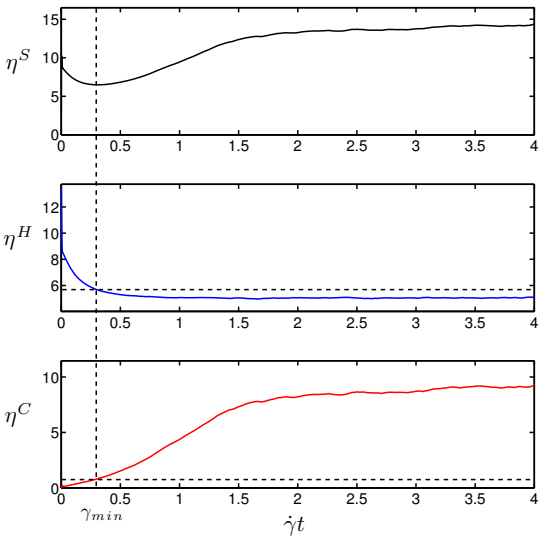

FIG. 8. The relative viscosity η^S of a suspension under shear reversal $\phi = 0.45$, $\mu = 0.5$, $h_r = 5.10^{-3}$ (top), together with the hydrodynamic contribution η^H (middle) and contact contribution η^C (bottom) as a function of shear strain $\dot{\gamma}t$.

At the beginning of this long time transient (Fig. 8), the contact forces have relaxed, and the contact contribution to the viscosity approximately vanishes. The hydrodynamic contribution is larger than its value before shear reversal (i.e its steady value). This can be qualitatively understood by considering contacting particles before shear reversal ($t = 0^-$, Fig. 9(a)) and after contact force relaxation ($\dot{\gamma}t \approx \dot{\gamma}\tau_s$, Fig. 9(c)). For the sake of simplicity, a particle pair with normal forces is displayed, without loss of generality. Before shear reversal (or alternatively at the end of the transient), the pair is aligned in the compressional quadrant, according to shear-induced microstructure in the moderately concentrated suspensions of interest in the present paper [17, 18]. The contact contribution to the viscosity is large and positive due to repulsive elastic forces. The same forces reduce the relative velocity of the particles, and thus reduce the hydrodynamic contribution. After contact force relaxation, the contact contribution vanishes, and the particles are now free to move away from each other under the action of the ambient shear flow. As a consequence of the lubrication forces that resist the relative motion, the hydrodynamic contribution to the viscosity is now larger, mostly due to the lubrication correction as noted in Sec. III A. It should be noted that the spatial arrangement of the particles is quite the same before shear reversal and after force relaxation, since the strain $\dot{\gamma}\tau_s$ keeps very small in the range of the parameters probed in the present paper (Sec. III D). However, the values of hydrodynamic viscosity at both step are not identical because the interparticle forces are not identical. Finally, in a very recent paper [32], similar simulations are performed, with similar qualitative conclusions. In particular, the initial decrease of the hydrodynamic contribution is explained in the same way. To support this explanation, the authors splitted the hydrodynamic (i.e. lubrication in their work) contribution in two part, corresponding to the particle pairs where the particles respectively move closer to or away from each other. They show that the initial high hydrodynamic contribution is due to the particles moving away from each other.

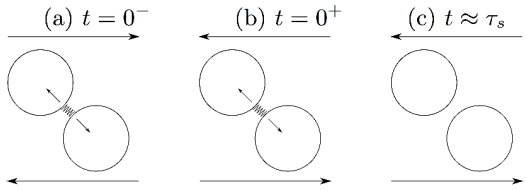

FIG. 9. Sketch of a particle pair aligned in the compressional quadrant of the initial ambient shear flow (a) before shear reversal (b) just after shear reversal (c) after contact force relaxation.

As displayed in Fig. 8, the suspension viscosity minimum originates in the competition between the decrease of the hydrodynamic contribution, due to the separation of the initially close particles, and the increase of the contact contribution due to the re-building of the force network. A striking feature here is that the hydrodynamic viscosity decrease is much faster than the contact viscosity increase. As a consequence, as the strain γ_{min}

is reached, η^H is close to its steady value while η^C is still close to 0. It is quite surprising, since the spatial arrangement of the particles, together with the force network are very different at $\dot{\gamma}t = \gamma_{min}$ and in steady shear, while the hydrodynamic viscosity takes similar values. This means that as the force network re-builds, and as the particles come closer to each other in the compressional quadrant of the ambient flow, their relative velocity decreases, resulting in an approximately constant hydrodynamic viscosity. This feature may be related to the property that the viscosity of a random suspension is close to the steady hydrodynamic contribution, as noted in Sec. III B.

An important consequence is that the suspension viscosity $\eta^S_{min} = \eta^H(\gamma_{min}) + \eta^C(\gamma_{min})$ seems to be quite close to the steady hydrodynamic viscosity η^H_{steady}, so that the difference $\eta^S_{steady} - \eta^S_{min}$ is expected to be close to the steady contact viscosity η^C_{steady}. In order to investigate this connection in a quantitative way, $\eta^S_{steady} - \eta^S_{min}$ is displayed in Fig. 10 as a function of the steady contact contribution to the viscosity η^C_{steady} for all values of the parameters ϕ, h_r/a and μ investigated in the present study. Both quantities are proportional with a very good

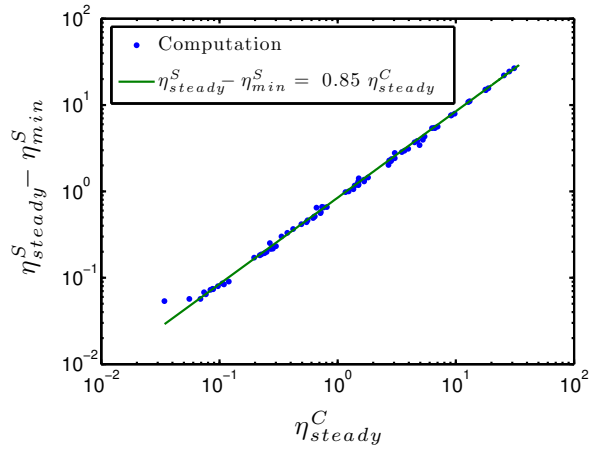

FIG. 10. Difference between steady and minimum suspension viscosity $\eta^S_{steady} - \eta^S_{min}$ as a function of steady contact viscosity η^C_{steady}. $0.25 \leq \phi \leq 0.5$, $h_r/a = 5.10^{-3}$; 10^{-2} ; 2.10^{-2}, $\mu = 0$; 0.3 ; 0.5 ; 1.

correlation over 3 orders of magnitude. It is not clear to us why this very simple correlation holds over a so wide contact viscosity range. The proportionality constant 0.85 may depend on the contact law between particles, even though it holds for frictionless and frictional particles as well.

Nevertheless, from an experimental point of view, this correlation may be useful, since it allows estimating the steady contact viscosity from a shear reversal experiment. In particular, this viscosity difference may be compared to the suspension steady viscosity. Figure 11 displays the ratio $(\eta^S_{steady} - \eta^S_{min})/\eta^S_{steady}$ as a function of the reduced volume fraction ϕ/ϕ^* from the simulations together with experimental measurements. Concerning the simulations, different symbols indicate different friction coefficient values. The experimental data are taken from earlier measurements in suspensions of PMMA particles in a Newtonian liquid, with particle radius 15.5 μm and apparent jamming volume fraction $\phi^* \approx 0.53$ [27]. Except for the case $\mu = 0$, all simulation results and experimental measurements approximately collapse on the same curve. At low volume fraction, the contact contribution to the steady viscosity vanishes, while the total suspension viscosity keeps finite. A high volume fraction, the contact viscosity is increasingly predominant. Finally, in a very recent paper where experimental transients in shear-thickening suspensions were measured [58], the contact contribution in shear-thickening suspensions was experimentally estimated using a relation roughly similar to the correlation in Fig. 10. To be specific, Lin et al. [58] took η_{init} for the hydrodynamic contribution to the steady viscosity, since their experiments do not display the initial decrease of the viscosity, but instead only a large scale increase up to the steady value. This choice for the hydrodynamic contribution was validated using simulations, that were further developed in [32]. Actually, as noted above, their simulations show the same nonmonotonic transient as in the present work, with the same qualitative explanation. The lack of such an initial viscosity decrease in the experiments may be explained by particular soft interactions, as further explored by Ness and Sun [32].

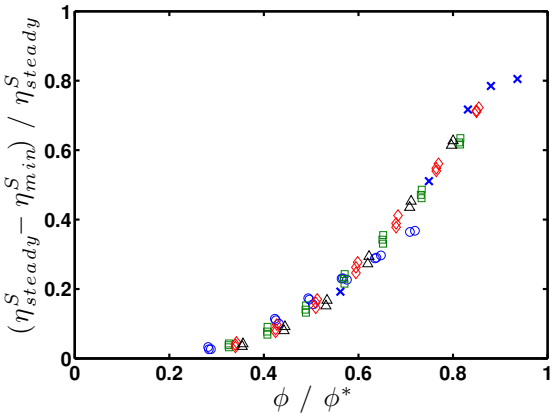

FIG. 11. Difference between steady and minimum suspension viscosity $\eta^S_{steady} - \eta^S_{min}$ to the steady η^S_{steady} suspension viscosity as a function of reduced volume fraction ϕ/ϕ^*. Simulations with $h_r/a \in [5.10^{-3}$; 10^{-2} ; $2.10^{-2}]$ and $\phi \in [0.25$; 0.3 ; 0.35 ; 0.4 ; 0.45 ; 0.5]: ($\circ$) $\mu = 0$, ($\square$) $\mu = 0.3$, ($\Diamond$) $\mu = 0.5$, ($\triangle$) $\mu = 0.7$, ($\times$) Experiments $\phi^* = 0.53$ - a = 15.5 μm [27].

The suspension viscosity goes to a minimum at the strain γ_{min}. Since this quantity can be easily measured in experiments, at least for moderate solid volume fraction, its variation with the simulation parameters deserves a few words. According to Fig. 12, γ_{min} (open symbols) decreases as the volume fraction increases, which

is quite intuitive and has been already noted in experiments [24, 26, 27]. In addition, γ_{min} decreases as the friction coefficient increases (Fig. 12(a)), or as the roughness height increases (Fig. 12(b)). A deep understanding

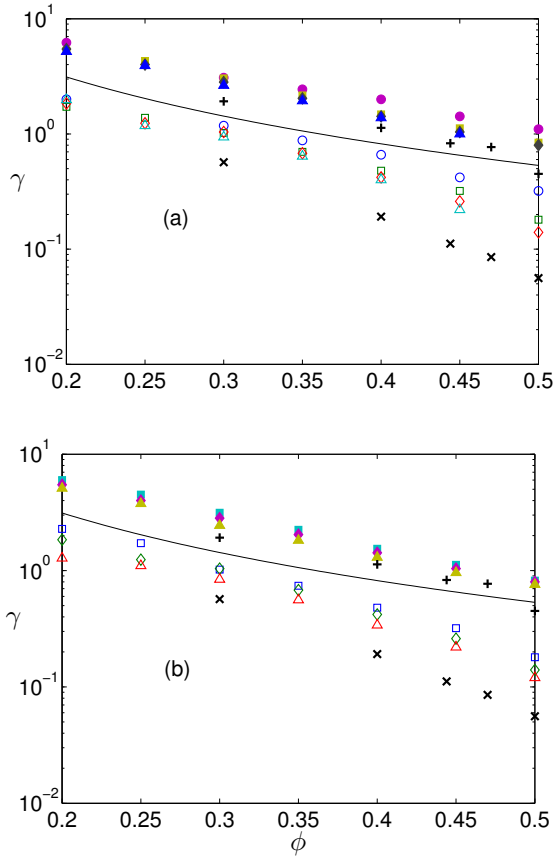

FIG. 12. Strain γ_{min} for the minimum viscosity (open symbols) and $\gamma_{0.5}$ (filled symbols, Eq. (26)) as a function of volume fraction ϕ (a) Different values of the friction coefficient (o) $\mu = 0$; (□) $\mu = 0.3$; (◇) $\mu = 0.5$; (△) $\mu = 1$, $h_r/a = 10^{-2}$ (b) Different values of the roughness height (□) $h_r/a = 5.\ 10^{-3}$; (◇) $h_r/a = 10^{-2}$; (△) $h_r/a = 2.\ 10^{-2}$, μ=0.5. (×) γ_{min} from experiments [27], (+) $\gamma_{0.5}$ from experiments [27], (−) Power law fit from [11] $\gamma_{c,P} = 0.14\ \phi^{-1.93}$.

of these trends is not easy, since the passage through a minimum involves the decrease of the hydrodynamic contribution together with the increase of the contact viscosity. Thus the particular value of γ_{min} is expected to depend on the relaxation strain and variation amplitude of both contributions. Nevertheless, the simulation results compare well with the experimental measurements from [27] (displayed as (×) in Fig. 12), though the latter are a bit under the former, suggesting a higher friction coefficient than 1 (in agreement with the low jamming volume fraction $\phi^* \approx 0.53$ that was measured) or (and) a larger roughness height than 2.10^{-2} a in the experiments. Concerning the experiments, it should be noted that the strain resolution is approximately 0.05 for the largest volume fractions $\phi = 0.47 - 0.5$, i.e. close to γ_{min}. As a consequence, the values of γ_{min} in this volume fraction range can only be estimated.

In the increasing part of the transient, the rebuild of the force network occurs over the typical strain $\gamma_{0.5}$ (Eq. (26)) that is displayed in Fig. 12 (filled symbol), together with its experimental counterpart from [27]. It turns out that $\gamma_{0.5}$ follows the same trends as γ_{min}. In particular, the data from the simulations overestimate the experimental results (displayed as (+)), which deserves the same explanation as previously. Since $\gamma_{0.5}$ may be understood as the strain that is necessary for the particles to irreversibly rearrange during the transient, it is worth comparing it to the critical strain measured by Pine et al. [11] in non-Brownian suspensions submitted to an oscillatory shear. In this paper, they showed that the particles return to their original position after one or more cycles only if the strain amplitude does not exceed a critical strain, denoted here by $\gamma_{c,P}$. In the large amplitude regime, the particles continuously undergo an irreversible random-walk. The power-law fit to the data of Pine et al. [11] is displayed in Fig.12 (solid line). As expected $\gamma_{c,P}$ shares the same qualitative evolution with the volume fraction and the same order of magnitude as $\gamma_{0.5}$.

D. Short strain dynamics

As explained in Sec. III A, the viscosity undergoes an instantaneous jump from $\eta^S_{(0-)}$ to $\eta^S_{(0+)}$, followed by a relaxation to η^S_{init} where the contact contribution approximately vanishes. The dynamics at times immediately after shear reversal, $0^+ \leq t \leq \tau_s$ is determined by the relaxation of the contact forces, as briefly mentioned above. By looking at the graph in the insets of Fig. 3, we note that at $t = 0$ the contact contribution changes sign but keeps exactly the same magnitude. This is not surprising: at shear reversal ($t = 0$), the contact forces between particles, that only depend on particle positions, do not vary, but their action switches from resistive to propulsive once the flow is reversed (Fig. 9(a-b)). Thus their contribution to the viscosity is merely reversed. Simultaneously, the hydrodynamic contribution dramatically increases (Fig. 3, $t = 0^+$). Again, this is explained by the simple physical picture in Fig. 9: before shear reversal, the action of the imposed flow is balanced by the repulsive contact forces (Fig. 9(a)). The relative velocities between neighboring particles are small, so that lubrication forces are small. But after shear reversal, both the contact forces and the imposed flow tend to separate particles (Fig. 9(b)) ; as a consequence, lubrication forces instantaneously jump to higher values, resulting in this large increase of the hydrodynamic viscosity (almost exclusively lubrication corrections). The net effect on the suspension viscosity is the instantaneous step from $\eta^S_{(0-)}$

to $\eta^S_{(0^+)}$. Then, in a short but finite time, the contact forces relax towards zero: particle surfaces mostly move to distances bigger than the roughness h_r, so that contacts vanish (Fig. 9(c)). Then, η^S is mostly given by its hydrodynamic components. This happens in a characteristic time τ_s determined by the relaxation of contact forces.

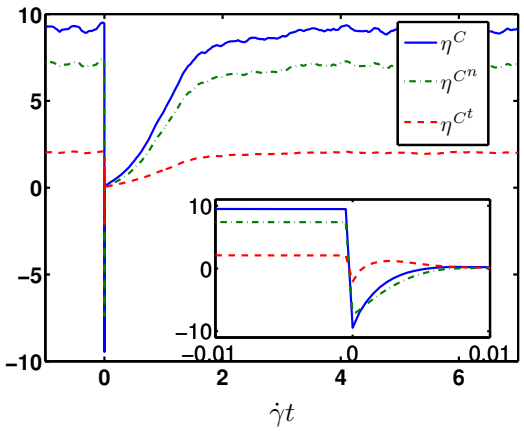

FIG. 13. Contact viscosity η^C together with the normal force η^{Cn} and tangential force η^{Ct} contributions as a function of shear strain $\dot\gamma t$

Figure 13 displays the transient evolution of the contact viscosity together with the contribution to the contact viscosity from the normal and tangential forces. They both vanish after the time $\dot\gamma\tau_s$ and grow slowly to their steady value with the same characteristic time. During the fast relaxation, the normal force contribution goes to zero without changing sign, in agreement with the idea that the non linear spring in the direction of the particle centers simply relaxes. The tangential contribution relaxes in a shorter time, and changes sign before complete vanishing : after shear reversal, the tangential spring relaxes due to the reversed relative tangential motion between particle surfaces and is stretched back before the contact vanishes due do relative normal motion. The (positive) residual viscosity for the tangential force contribution is at most 5 % of it steady value, for the largest volume fraction and friction coefficient, and 2 % for the normal contribution, so that the overall (positive) residual contact viscosity is at most 3 % of its steady value. As noted in the following (Sec. III D 2), the tangential forces contribution keeps quite small compared to the normal forces contribution.

We first focus on the determination of the relaxation strain $\dot\gamma\tau_s$ in Sec. III D 1. Then the relevant values of the viscosity at shear reversal will be addressed in Sec. III D 2.

1. *Determination of τ_s*

The relaxation strain $\dot\gamma\tau_s$ of the contact forces can be directly measured from the numerical results. It is here defined as the strain needed for the contact viscosity to relax to 5% of $\eta^C_{(t=0^+)}$ (Fig. 3). A subset of the computed values is displayed in fig.14 for the sake of clarity. $\dot\gamma\tau_s$ is found to weakly depend on the friction coefficient and roughness height at low volume fraction, with $\dot\gamma\tau_s \approx 6\ 10^{-3}$. The variations with the roughness height are a bit more significant as the volume fraction increases. It is found $3\ 10^{-3} \lesssim \dot\gamma\tau_s \lesssim 1.5\ 10^{-2}$ for all the conducted simulations, and most of values lie in the range $4\ 10^{-3}$ - $8\ 10^{-3}$.

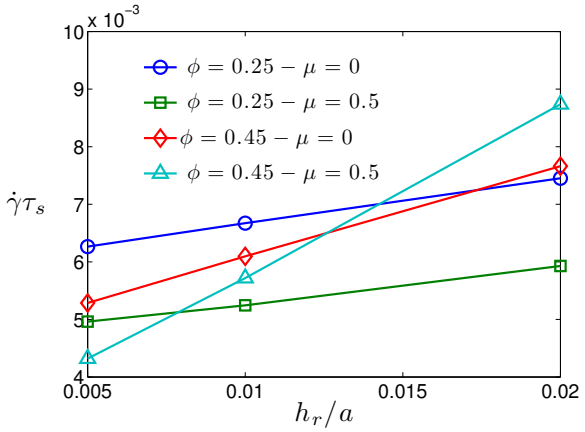

FIG. 14. Selected representative values of the reduced relaxation time $\dot\gamma\tau_s$ of particle normal forces as a function of particle roughness h_r/a.

A simple model based on the force balance for a particle pair can also be used to obtain a rough estimation of τ_s. Let us consider the motion of two particles in a fluid, with only normal contact forces for the sake of simplicity (Fig. 9(b-c)). Lubrication theory allows to evaluate the hydrodynamic force localized between the particles as a function of the separation distance δ:

$$F^{lub} \sim 6\pi\eta a^2 \frac{\dot\delta}{4\delta} \tag{27}$$

Besides this lubrication force, the external shear flow is responsible for a supplementary hydrodynamic force of approximate magnitude $6\pi\eta a^2\dot\gamma$ [52, 59], which is also the order of magnitude of the largest repulsive contact forces. The balance of all forces yields, in order of magnitude, the following relationship:

$$2\dot\gamma \sim \frac{\dot\delta}{4\delta} \tag{28}$$

If the typical distance between contacting particle surfaces is denoted by $\bar\delta$, the typical roughness compression $(h_r - \bar\delta)$ may be connected to the relaxation time

as $(h_r - \bar{\delta}) = \dot{\delta}\tau_s$. Taking $\delta \sim \bar{\delta}$, and recalling that $\bar{\epsilon} = (h_r - \bar{\delta})/h_r$, we obtain

$$\tau_s \dot{\gamma} \sim \frac{(h_r - \bar{\delta})}{8\bar{\delta}} \sim \frac{\bar{\epsilon}}{8(1-\bar{\epsilon})} \tag{29}$$

Equation (29) shows that the relaxation of the contact force is actually expressed by a characteristic strain that is a function of the typical roughness deformation $\bar{\epsilon}$. In the present work, $\bar{\epsilon} = \dot{\Gamma}^{2/3} = 0.01^{2/3} \sim 4.6\ 10^{-2}$ is kept constant while the parameters h_r/a and μ are varied (Sec. II F). As a consequence, Eq. (29) yields a single numerical constant for all simulations presented here $\dot{\gamma}\tau_s \sim 6 \cdot 10^{-3}$, in very good agreement with the numerical results. We admit that, in order that the validity of Eq. (29) might be completely checked, the dimensionless parameter $\dot{\Gamma}$ should be varied, which is nevertheless out of the scope of the present paper.

Finally, it must be kept in mind while using Eq. (29) that $\bar{\epsilon}$ depends on $\dot{\gamma}$ through Eq. (13): the larger the shear rate is, the more compressed are the particles. For that reason, in experiments where $\dot{\gamma}$ is varied, the relaxation time may change, approximately as $\dot{\gamma}^{-1/3}$. However, in the parameter range that is probed in the present paper, $\dot{\gamma}\tau_s \ll 1$, so that the dynamics for $0 \leq t \leq \tau_s$ may not be easily accessible in experiments.

2. *Viscosity steps at shear reversal*

The short time transient involves three different viscosity values, as already mentioned earlier: the viscosity before shear reversal $\eta^S_{(0^-)}$, which is the same as the steady viscosity η^S_{steady} except for the fluctuations, the viscosity just after shear reversal $\eta^S_{(0^+)}$ and η^S_{init} the viscosity after contact force relaxation extrapolated to $t = 0$. We may thus indentify two different viscosity steps, depending on the strain scale that is considered. A first step is undergone instantaneously at $t = 0$, namely $\eta^S_{(0^-)}$ - $\eta^S_{(0^+)}$. At a larger time scale ($t \gtrsim \tau_s$), another viscosity step may be evidenced, i.e. $\eta^S_{(0^-)}$ - η^S_{init}. In this section, a qualitative understanding of the steps is sought, together with quantitative information concerning their variation with the different physical parameters.

It turns out that both steps are connected. Fig. 15 displays the instantaneous step $\eta^S_{(0^-)}$ - $\eta^S_{(0^+)}$ as a function of $\eta^S_{(0^-)}$ - η^S_{init} for all values of the parameters probed in the present study. The former equals twice the latter with a very good correlation over the whole parameter range. This relation originates in the lack of inertia in the considered flows. To be more specific, using the linearity of Stokes equation, the flow before shear reversal at $t = 0^-$ can be split into two different flows that share the same particle positions as the original flow (Fig. 16, first line): a flow (I) driven by the ambient shear flow, without contact force between particles and a flow (II) driven by the same contact forces as in the original flow, but

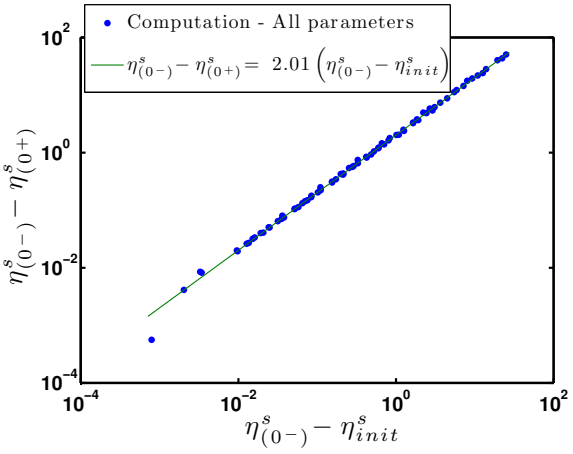

FIG. 15. Connection between the viscosity steps $(\eta^S_{0-} - \eta^S_{init})$ and $(\eta^S_{0-} - \eta^S_{0+})$. Parameter range: $0.2 \leq \phi \leq 0.5$, $0 \leq \mu \leq 1$, $5.10^{-3} \leq h_r/a \leq 2.10^{-2}$. Solid line: linear fit.

without ambient shear flow. This splitting is also easily expressed using the mobility formulation of the relation between particle velocity, angular velocity and stresslet on the one hand and the hydrodynamic force, torque and stresslet on the particles on the other hand [59] and is instrumental in performing Stokesian Dynamics computations [60]. As a consequence, the stress defined in Eq.

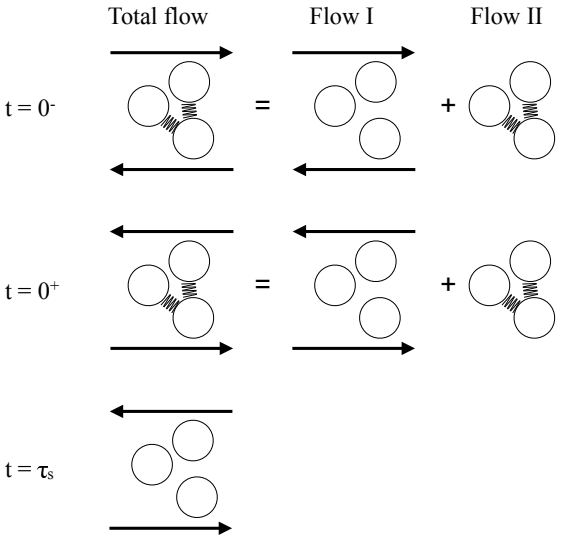

FIG. 16. Schematic view of the splitting of the flow into two flows driven either by the ambient shear flow (flow I) or the contact forces (flow II).

(20)-(22) is the sum of the stresses associated with each flow.

$$\mathbf{\Sigma}_{(t=0^-)} = \mathbf{\Sigma^I}_{(t=0^-)} + \mathbf{\Sigma^{II}}_{(t=0^-)} \tag{30}$$

The viscosity can be split in the same way:

$$\eta^S_{(0^-)} = \frac{\Sigma^I_{xy(t=0^-)} + \Sigma^{II}_{xy(t=0^-)}}{\eta\dot{\gamma}} = \eta^I + \eta^{II} \tag{31}$$

Thus η^I (resp. η^{II}) is defined as the viscosity associated to flow (I) (resp. II) at time t=0^-. It should be noted that η^I is hydrodynamic in nature, since no direct force applies between particles in the flow (I), while η^{II} is the sum of an hydrodynamic contribution and a contact contribution, the latter being the same as in the total flow.

This separation holds after shear reversal at time t=0^+ (Fig. 16, second line). The particle positions together with the contact forces are exactly the same as before shear reversal, and the ambient shear flow is reversed, so that the stress of flow (I) is reversed due to linearity of Stokes equation, while the stress of flow (II) is unchanged. As a consequence, the suspension viscosity reads now:

$$\begin{aligned}\eta^S_{(0^+)} &= \frac{\Sigma_{(t=0^+)}}{-\eta\dot{\gamma}} \\ &= \frac{-\Sigma^I_{xy(t=0^-)} + \Sigma^{II}_{xy(t=0^-)}}{-\eta\dot{\gamma}} \\ &= \eta^I - \eta^{II}\end{aligned} \tag{32}$$

After contact force relaxation (t=τ_s), the contact force approximately vanishes, so that $\mathbf{\Sigma}_{(t=\tau_s)} \approx \mathbf{\Sigma}^I_{(t=\tau_s)}$. Since the particle asperities are weakly compressed before shear reversal ($h_r - \bar{\delta} \ll h_r$ in Eq. (14)), the particles positions are approximately the same at $t = 0^-$ and $t = \tau_s$. As a consequence, due to linearity of Stokes equation, $\mathbf{\Sigma}^I_{(t=\tau_s)} \approx -\mathbf{\Sigma}^I_{(t=0^-)}$ and the viscosity after contact force relaxation reads:

$$\begin{aligned}\eta^S_{init} &\approx \frac{-\Sigma_{xy(t=0^+)}}{-\eta\dot{\gamma}} \\ &\approx \eta^I\end{aligned} \tag{33}$$

From Eq. (31)-(33), the viscosity steps read:

$$\begin{aligned}\eta^S_{(0^-)} - \eta^S_{(0^+)} &= 2\ \eta^{II} \\ \eta^S_{(0^-)} - \eta^S_{init} &\approx \eta^{II}\end{aligned} \tag{34}$$

while a second expression for the viscosity of flow (I) is available:

$$\eta^S_{(0^-)} + \eta^S_{(0^+)} = 2\ \eta^I \tag{35}$$

Eq. (34) accounts for the proportionality of the instantaneous viscosity step $\eta^S_{(0^-)} - \eta^S_{(0^+)}$ and the viscosity step at the time scale of contact force relaxation $\eta^S_{(0^-)} - \eta^S_{init}$ that is evidenced in Fig. 15. In the following, the term "viscosity step" denotes $\eta^S_{(0^-)} - \eta^S_{init}$. In addition, we have checked that Eq. (33) and (35) yield the same value for η^I.

Eq. (33) and (34) deserve a few comments. First, Eq. (34) directly connects the viscosity step to the viscosity associated with the flow (II) that is completely driven by the contact forces. According to Eq. (22), η^{II} is the sum of two contributions, respectively hydrodynamic and contact in nature. The contact contribution depends on the elastic contact forces between particles that push them apart. The induced flow, in turn, results in hydrodynamic forces that resist this motion. As a consequence, both contributions to the viscosity are expected to be qualitatively opposite, with a positive contact contribution and a negative hydrodynamic contribution. *A viscosity step occurs only if the balance is not perfect between both contributions, i.e. the contact contribution is larger than the hydrodynamic one in flow (II).*

In addition, Eq. (33) provides a physical picture for the viscosity after contact force relaxation η^S_{init}: it is *the viscosity that the suspension would exhibit with the same positional microstructure as in steady shear, but without contact force between particles.* As explained above, this statement is strongly supported by the fact that Eqs (33) and (35) yield the same value for η^I. In addition, simulations allow to directly compute η^I : for the particle positions at time $t = 0$ before shear-reversal, the forces can be canceled, and the flow computed. We have checked for a few values of the parameters ϕ, h_r/a and μ that the computed viscosity equals η^S_{init} within a few tenths of a percent.

Finally, it was previously mentioned that the hydrodynamic viscosity is larger after force relaxation ($t = \tau_s$) than before shear reversal ($t = 0^-$). From Fig. 16, or alternatively Eq. (31) and (33), it means that flow (I) and (II) have opposite hydrodynamic contributions to the stress, and, depending on volume fraction, with similar intensity. It is easily understood in a qualitative way: at $t = 0^-$, flow (I) brings the neighboring particles closer (in the compressional quadrant), with a lubrication flow between particles that resists this motion, while in flow (II) the contact forces separate the same particles, inducing a flow between them that acts to keep them together. The two flows are thus opposite, and their superposition ($t = 0^-$) results in a weak flow between particles, inducing a weak hydrodynamic contribution to the viscosity.

Eq. (34) suggests that the viscosity step should be compared to the steady contact viscosity, since flow (II) is driven by the contact forces. Fig. 17 displays the ratio of the viscosity step to the steady contact viscosity as a function of solid volume fraction for different values of the friction coefficient. Two different regimes may be identified. At low volume fraction, the viscosity step is quite small compared to the steady contact viscosity, suggesting that in flow (II), the hydrodynamic contribution approximately balances the contact contribution. As the friction coefficient increases, this balance is less effective. As the solid volume fraction increases, the ratio of the viscosity step to the steady contact viscosity increases, especially for the larger values of the friction coefficient, meaning that in flow (II) the hydrodynamic viscosity turns smaller compared to the contact viscosity.

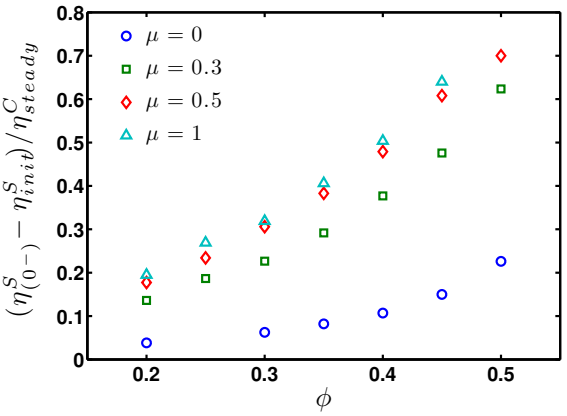

FIG. 17. Ratio of the jump in relative viscosity $(\eta^S_{0-} - \eta^S_{init})$ to the steady contact viscosity η^C_{steady}. $h_r/a = 5.10^{-3}$.

Particle pair idealization

The low volume fraction limit may be understood considering a pair of contacting particles submitted to shear reversal. In that case, the stresslet of the particle pair associated to flow (II) can be computed from the two-particle mobility matrix. Its expression in the limit of nearly touching spheres is shortly derived in appendix A. The distance between particle surfaces is supposed to be exactly $\delta = h_r$, since the roughness typical compression is small (Eq. 14 and Sec. II F). From Eq. A8, together with Eq. (22) and (24), the viscosity associated to flow (II) is linearly related to the normal and tangential contact force contributions to the viscosity η^{Cn} and η^{Ct}:

$$\eta^{II}_{pair} = \left(1 - \frac{N\left(h_r/a\right)}{1 + h_r/2a}\right)\eta^{Cn} + \left(1 - \frac{T\left(h_r/a\right)}{1 + h_r/2a}\right)\eta^{Ct} \tag{36}$$

where $\eta^{Cn} + \eta^{Ct}$ is the contact contribution to the viscosity before shear reversal (or equivalently the steady contact viscosity) and the remaining terms are the hydrodynamic contribution to flow (II). As explained in the appendix (Fig. 21), in the range of roughness that is considered in the present study, the normal force contribution is closely balanced by its hydrodynamic counterpart $[1 + h_r/2a - N\left(h_r/a\right)] \ll 1$, which is not the case for the tangential force contribution. This is in qualitative agreement with Fig. 17, where the ratio of the viscosity step to the steady contact viscosity is smaller in the case of frictionless particles. From Eq. (36), it is clear that the viscosity step may strongly depend on the relative importance of the normal and tangential forces contribution in the contact viscosity. Surprisingly, the ratio of the tangential contribution to the total contact viscosity from the simulations hardly depends on the roughness height or even on the solid concentration, but only on the friction coefficient, as shown in Fig. 18. As mentioned previously, even though the fraction of the tangential force contribution can be as high as 25% for the largest friction coefficient considered here, the strong increase of the contact contribution induced by friction is not only due to the addition of the tangential force contribution, but rather to a large increase of the normal force contribution. Now, using the simulation result in Fig. 18, Eq. (36) reads:

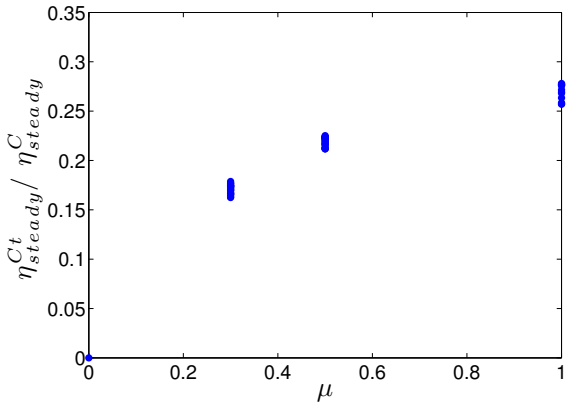

FIG. 18. Ratio of the tangential contribution η^{Ct}_{steady} to the total contact η^C_{steady} viscosity as a function of friction coefficient μ. $0.2 \leq \phi \leq 0.5$, $5.10^{-3} \leq h_r/a \leq 2.10^{-2}$.

$$\eta^{II}_{pair} = \eta^C \left[\left(1 - \frac{N\left(h_r/a\right)}{1 + h_r/2a}\right)\left(1 - \beta_t(\mu)\right) + \left(1 - \frac{T\left(h_r/a\right)}{1 + h_r/2a}\right)\beta_t(\mu)\right] \tag{37}$$

with $\beta_t(\mu) = \eta^{Ct}/\eta^C$. The ratio of the viscosity step to the steady contact viscosity is thus expected to depend both on the roughness height and the friction coefficient. For a given value of h_r/a, as the friction coefficient increases, the relative contribution β_t of the tangential forces increases and the viscosity ratio η^{II}_{pair}/η^C is expected to increase, in agreement with Fig. 17.

The viscosity step from the simulations is now compared to the value that is expected from the particle pair model (Eq. 36) where the normal and tangential forces contributions are taken from the simulations in steady shear. In Fig. 19, the ratio of viscosity step $\eta^S_{(0^-)} - \eta^S_{init}$ to η^{II}_{pair} is displayed for different values of the friction coefficient (Fig. 19(a)) and of the roughness height (Fig.

19(b)). As the volume fraction decreases, the viscosity

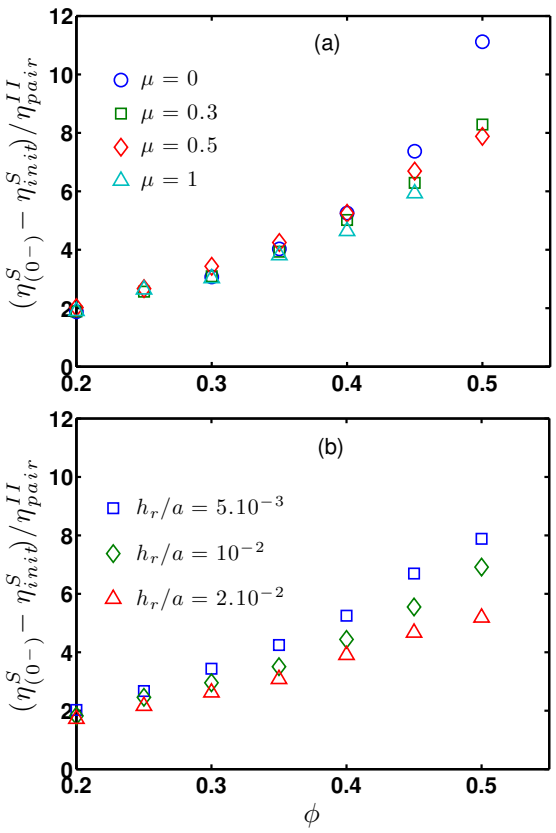

FIG. 19. Ratio of the viscosity step $\eta^S_{(0-)} - \eta^S_{init}$ to the expected step from particle pair model η^{II}_{pair} (Eq. 36) as a function of solid volume fraction (a) $h_r/a = 5.10^{-3}$ (b) $\mu = 0.5$

step approaches the value that is expected from the particle pair model. It should be noted that both numerator and denominator of the ratio go to zero with the volume fraction, and are very small at $\phi = 0.2$.

However, as the volume fraction increases, the computed viscosity step grows larger compared to the value that is predicted by the simple particle pair model. It means that the partial balance of the hydrodynamic and contact contribution to the viscosity of flow (II) does not hold anymore, as already noted in Fig. 17, and the contact contribution may be much larger than the hydrodynamic contribution. The reason why this happens is not totally clear to us. The long range multibody hydrodynamic interactions have been neglected in the simple model developed in Appendix A. However, prediction of the qualitative effect of those interactions on the relative weight of the hydrodynamic and contact contribution is not easy.

IV. CONCLUSION

In this paper, shear reversal in non-Brownian suspensions has been simulated using the Force Coupling Method, that includes long range hydrodynamic interactions, short range lubrication interactions together with contact force between particles. In particular, the roughness of the particle surface, as well as the friction between particles were taken into account. Inspection of the steady part of the transient reveals a strong influence of the friction coefficient μ on the contact contribution to the viscosity, as already shown by Gallier et al. [18]. In addition, the apparent jamming volume fraction ϕ^* significantly depends on μ, while it hardly changes with the surface roughness height h_r/a.

Separate inspection of the hydrodynamic and contact contribution to the viscosity provides a deeper insight into the transient. After contact force relaxation, the hydrodynamic contribution is high, while the contact contribution vanishes. The hydrodynamic contribution undergoes a fast relaxation to its steady value, while the increase of the contact part, connected to the building of the contact network, is slower. As a consequence, the difference between the steady viscosity and the minimum viscosity is proportional to the steady contact viscosity, whatever the friction coefficient and surface roughness height in the range probed in the present article. From an experimental point of view, this allows estimating the contact part of the steady viscosity.

After shear reversal, the contact forces relax over a strain that is approximately given by the typical relative compression of the asperities, which is kept constant throughout this study. This typical strain is approximately $\dot{\gamma}\tau_s \sim 5.10^{-3} - 10^{-2}$. To understand the apparent viscosity step at shear reversal $\eta^S_{0-} - \eta^S_{init}$, the flow before shear reversal can be split into two different flows that share the same particle positions as the original flow: a flow (I) driven by the ambient shear flow, without contact force between particles and a flow (II) driven by the same contact force network as in the original flow, but without ambient shear flow. The viscosity step is related to the stress of flow (II). For the smallest volume fraction, this step is much smaller than the contact contribution to the steady viscosity, in agreement with a simple particle pair model. As the volume fraction increases, the viscosity step is comparable to the steady contact viscosity. It is thus expected that the step tends to the contact viscosity as the volume fraction tends to the jamming volume fraction. Finally, this separation into two different flows apparently makes sense in the context of shear reversal of a suspension. However, the relevance of such a separation in the more general field of suspension rheology is still an open question to us.

ACKNOWLEDGMENTS

This work was granted access to the HPC and visualization resources of "Centre de Calcul Interactif" hosted by "Université Nice Sophia Antipolis"

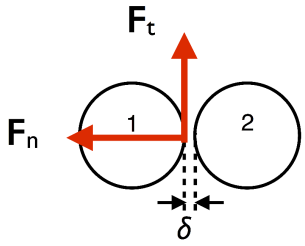

FIG. 20. Pair of contacting particles

Appendix A: Stresslet step at shear reversal for a particle pair

In this appendix, the total deviatoric stresslet, with both contact and hydrodynamic contributions, is computed for a contacting particle pair (flow (II) defined in Sec. III D 2). The separation vector between particles centers is denoted by $\mathbf{r} = \mathbf{x}_2 - \mathbf{x}_1 = r\mathbf{d}$ where $r = 2a + \delta = a(2 + \xi)$ is the distance between particles. The force $\mathbf{F}$ exerted on particle 1 is the sum of the normal component $\mathbf{F}_n$, i.e. along the direction of the particle centers, and the tangential component $\mathbf{F}_t$. The deviatoric stresslet of particle 1 is the sum of two contributions. First, the contact contribution from Eq. (20) can be split into the contributions of normal and tangential forces:

$$\mathbf{S}_1^c = (1+\xi/2)\left[\left(\frac{\mathbf{F}_n\otimes a\mathbf{d}+a\mathbf{d}\otimes\mathbf{F}_n}{2}-\frac{\mathbf{F}_n.a\mathbf{d}}{3}\mathbf{I}\right)+\frac{\mathbf{F}_t\otimes a\mathbf{d}+a\mathbf{d}\otimes\mathbf{F}_t}{2}\right] \tag{A1}$$

where $\mathbf{I}$ is the unity tensor. Particles inertia is neglected, so that the hydrodynamic force and torque on particles 1 and 2 read:

$$\begin{aligned}\mathbf{F}_1^h &= -\mathbf{F}_2^h = -\mathbf{F}_n - \mathbf{F}_t \\ \mathbf{T}_1^h &= \mathbf{T}_2^h = -(1+\xi/2)\, a\mathbf{d}\times\mathbf{F}_t\end{aligned} \tag{A2}$$

As a consequence, the hydrodynamic stresslet is written using the relevant mobility matrices $\mathbf{g}_{\alpha\beta}$ and $\mathbf{h}_{\alpha\beta}$ with the notation of Ref. [59].

$$\begin{aligned}\mathbf{S}_1^h =& -(\mathbf{g}_{11}-\mathbf{g}_{12})\cdot(\mathbf{F}_n+\mathbf{F}_t) \\ & -(1+\xi/2)(\mathbf{h}_{11}+\mathbf{h}_{12})\cdot(a\mathbf{d}\times\mathbf{F}_t)\end{aligned} \tag{A3}$$

After a few lines of calculus, the hydrodynamic stresslet on particle 1 follows:

$$\begin{aligned}\mathbf{S}_1^h =& -N(\xi)\left(\frac{\mathbf{F}_n\otimes a\mathbf{d}+a\mathbf{d}\otimes\mathbf{F}_n}{2}-\frac{\mathbf{F}_n.a\mathbf{d}}{3}\mathbf{I}\right) \\ & -T(\xi)\,\frac{\mathbf{F}_t\otimes a\mathbf{d}+a\mathbf{d}\otimes\mathbf{F}_t}{2}\end{aligned} \tag{A4}$$

with

$$\begin{aligned}N(\xi) &= \frac{x_{11}^g(\xi)-x_{12}^g(\xi)}{a} \\ T(\xi) &= 2\,\frac{y_{11}^g(\xi)-y_{12}^g(\xi)+a(1+\xi/2)\left(y_{11}^h(\xi)+y_{12}^h(\xi)\right)}{a}\end{aligned} \tag{A5}$$

Using the nearly touching sphere approximation for the mobility functions $x_{\alpha\beta}^g$, $y_{\alpha\beta}^g$ and $y_{\alpha\beta}^h$ [59], the analytical expressions for the functions $N(\xi)$ and $T(\xi)$ follow:

$$\begin{aligned}N(\xi) &\approx 1 - 3.5774\,\xi \\ T(\xi) &\approx 2\,\frac{0.5\ \log(\xi^{-1})^2+1.901\ \log(\xi^{-1})-2.0969}{log(\xi^{-1})^2+6.0425\ \log(\xi^{-1})+6.32549} \\ &\quad +\xi\,\frac{0.2972\ \log(\xi^{-1})^2+1.1526\ \log(\xi^{-1})-1.1415}{\log(\xi^{-1})^2+6.0425\ \log(\xi^{-1})+6.32549}\end{aligned} \tag{A6}$$

Thus the total stresslet of the particle pair is written:

$$\begin{aligned}\mathbf{S}_{pair} &= 2\ (1+\xi/2-N(\xi))\left(\tfrac{\mathbf{F}_n\otimes a\mathbf{d}+a\mathbf{d}\otimes\mathbf{F}_n}{2}-\tfrac{\mathbf{F}_n.a\mathbf{d}}{3}\mathbf{I}\right) \\ &\quad +2\ (1+\xi/2-T(\xi))\,\tfrac{\mathbf{F}_t\otimes a\mathbf{d}+a\mathbf{d}\otimes\mathbf{F}_t}{2} \\ &= \left(1-\tfrac{N(\xi)}{1+\xi/2}\right)\mathbf{S}_{pair}^{Cn}+\left(1-\tfrac{T(\xi)}{1+\xi/2}\right)\mathbf{S}_{pair}^{Ct}\end{aligned} \tag{A7}$$

where $\mathbf{S}_{pair}^{Cn}$ and $\mathbf{S}_{pair}^{Ct}$ respectively stand for the normal and tangential force contributions to the contact stresslet. Both functions $N(\xi)$ and $T(\xi)$ go to 1 as ξ goes to 0. This means that, as the distance between particle surfaces vanishes, the hydrodynamic stresslet of the pair more closely approaches the contact stresslet, i.e. the hydrodynamic forces are localized at contact point. However, as usual, the function $T(\xi)$ that is connected to the relative tangential motion of the particles depends on $\log(\xi^{-1})$, and consequently goes slower to 1 compared to $N(\xi)$. This feature is clearly evidenced in Fig. 21. For instance, when the normalized distance between particle

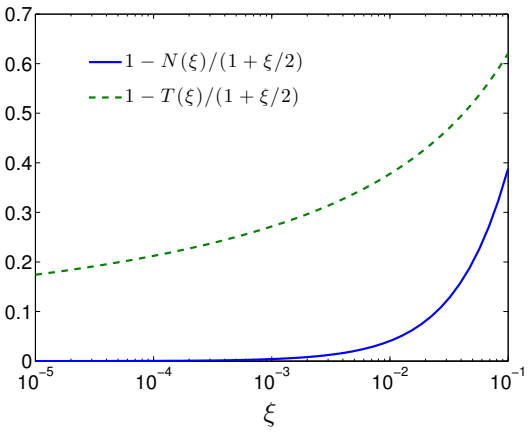

FIG. 21. Functions that relate the total stresslet to the contact stresslet of the pair (Eq. A8) as a function of the normalized distance between particle surfaces $\xi = r/a - 2$.

surfaces is as small as ξ=5.10^{-3}, the ratio of the hydrodynamic stresslet to the contact stresslet due to tangential force is $-T(\xi)/(1+\xi/2) \approx -0.66$, while the corresponding ratio for the normal force is much closer to -1: $-T(\xi)/(1+\xi/2) \approx -0.9797$.

[1] Jonathan J Stickel and Robert L Powell, "Fluid mechanics and rheology of dense suspensions," Annual Review of Fluid Mechanics **37**, 129–149 (2005).

[2] Jeffrey F Morris, "A review of microstructure in concentrated suspensions and its implications for rheology and bulk flow," Rheologica Acta **48**, 909–923 (2009).

[3] Morton M Denn and Jeffrey F Morris, "Rheology of non-brownian suspensions," Annual review of chemical and biomolecular engineering **5**, 203–228 (2014).

[4] Guillaume Ovarlez, François Bertrand, and Stéphane Rodts, "Local determination of the constitutive law of a dense suspension of noncolloidal particles through magnetic resonance imaging," Journal of Rheology **50**, 259–292 (2006).

[5] Isidro E Zarraga, Davide A Hill, and David T Leighton Jr, "The characterization of the total stress of concentrated suspensions of noncolloidal spheres in newtonian fluids," Journal of Rheology **44**, 185–220 (2000).

[6] Étienne Couturier, François Boyer, Olivier Pouliquen, and Élisabeth Guazzelli, "Suspensions in a tilted trough: second normal stress difference," Journal of Fluid Mechanics **686**, 26–39 (2011).

[7] François Boyer, Olivier Pouliquen, and Élisabeth Guazzelli, "Dense suspensions in rotating-rod flows: normal stresses and particle migration," Journal of Fluid Mechanics **686**, 5–25 (2011).

[8] Talib Dbouk, Laurent Lobry, and Elisabeth Lemaire, "Normal stresses in concentrated non-brownian suspensions," Journal of Fluid Mechanics **715**, 239–272 (2013).

[9] S Garland, G Gauthier, J Martin, and JF Morris, "Normal stress measurements in sheared non-brownian suspensions," Journal of Rheology **57**, 71–88 (2013).

[10] Andrea W Chow, Steven W Sinton, Joseph H Iwamiya, and Thomas S Stephens, "Shear-induced particle migration in couette and parallel-plate viscometers: Nmr imaging and stress measurements," Physics of Fluids **6**, 2561–2576 (1994).

[11] D. J. Pine, J. P. Gollub, J. F. Brady, and A. M. Leshansky, "Chaos and threshold for irreversibility in sheared suspensions," Nature **438**, 997–1000 (2005).

[12] Indresh Rampall, JEFFREY R Smart, and David T Leighton, "The influence of surface roughness on the particle-pair distribution function of dilute suspensions of non-colloidal spheres in simple shear flow," Journal of Fluid Mechanics **339**, 1–24 (1997).

[13] A Sierou and JF Brady, "Rheology and microstructure in concentrated noncolloidal suspensions," Journal of Rheology **46**, 1031–1056 (2002).

[14] C Gao, SD Kulkarni, JF Morris, and JF Gilchrist, "Direct investigation of anisotropic suspension structure in pressure-driven flow," Physical Review E **81**, 041403 (2010).

[15] Frédéric Blanc, François Peters, and Elisabeth Lemaire, "Experimental signature of the pair trajectories of rough spheres in the shear-induced microstructure in noncolloidal suspensions," Physical review letters **107**, 208302 (2011).

[16] Xiang Cheng, Jonathan H McCoy, Jacob N Israelachvili, and Itai Cohen, "Imaging the microscopic structure of shear thinning and thickening colloidal suspensions," Science **333**, 1276–1279 (2011).

[17] F. Blanc, E. Lemaire, A. Meunier, and F. Peters, "Microstructure in sheared non-brownian concentrated suspensions," Journal of Rheology **57**, 273 (2013).

[18] S. Gallier, E. LemE. Lemaire. Peters, and L. Lobry, "Rheology of sheared suspensions of rough frictional particles," Journal of Fluid Mechanics **757**, 514–549 (2014).

[19] German Drazer, Joel Koplik, Boris Khusid, and Andreas Acrivos, "Deterministic and stochastic behaviour of non-brownian spheres in sheared suspensions," Journal of Fluid Mechanics **460**, 307–335 (2002).

[20] Helen J Wilson and Robert H Davis, "Shear stress of a monolayer of rough spheres," Journal of Fluid Mechanics **452**, 425–441 (2002).

[21] R. Seto, R. Mari, J. F. Morris, and M M. Denn, "Discontinuous shear thickening of frictional hard-sphere suspensions," Physical Review Letters **111**, 218301 (2013).

[22] Romain Mari, Ryohei Seto, Jeffrey F Morris, and Mor-

ton M Denn, "Shear thickening, frictionless and frictional rheologies in non-brownian suspensions," Journal of Rheology **58**, 1693–1724 (2014).
[23] Matthieu Wyart and ME Cates, "Discontinuous shear thickening without inertia in dense non-brownian suspensions," Physical Review Letters **112**, 098302 (2014).
[24] F. Gadala-Maria and Andreas Acrivos, "Shear-induced structure in a concentrated suspension of solid spheres," Journal of Rheology **24**, 799–814 (1980).
[25] Takatsune Narumi, Howard See, Yuichi Honma, Tomiichi Hasegawa, Tsutomu Takahashi, and Nhan Phan-Thien, "Transient response of concentrated suspensions after shear reversal," Journal of Rheology **46**, 295–305 (2002).
[26] Venkata Giri Kolli, Emily J. Pollauf, and Francis Gadala-Maria, "Transient normal stress response in a concentrated suspension of spherical particles," Journal of Rheology **46**, 321–334 (2002).
[27] F. Blanc, F. Peters, and E. Lemaire, "Local transient rheological behavior of concentrated suspensions," Journal of Rheology **55**, 835–854 (2011).
[28] Asimina Sierou and John F Brady, "Accelerated stokesian dynamics simulations," Journal of Fluid Mechanics **448**, 115–146 (2001).
[29] Jonathan M Bricker and Jason E Butler, "Correlation between stresses and microstructure in concentrated suspensions of non-brownian spheres subject to unsteady shear flows," Journal of Rheology **51**, 735–759 (2007).
[30] Jonathan J Stickel, Ronald J Phillips, and Robert L Powell, "Application of a constitutive model for particulate suspensions: Time-dependent viscometric flows," Journal of Rheology **51**, 1271–1302 (2007).
[31] Jonathan J Stickel, Ronald J Phillips, and Robert L Powell, "A constitutive model for microstructure and total stress in particulate suspensions," Journal of Rheology **50**, 379–413 (2006).
[32] Christopher Ness and Jin Sun, "Two-scale evolution during shear reversal in dense suspensions," Physical Review E **93**, 012604 (2016).
[33] Victor Breedveld, Dirk van den Ende, Robert Jongschaap, and Jorrit Mellema, "Shear-induced diffusion and rheology of noncolloidal suspensions: Time scales and particle displacements," The Journal of Chemical Physics **114**, 5923–5936 (2001).
[34] Takatsune Narumi, Howard See, Atsushi Suzuki, and Tomiichi Hasegawa, "Response of concentrated suspensions under large amplitude oscillatory shear flow," Journal of Rheology **49**, 71–85 (2005).
[35] Jonathan M Bricker and Jason E Butler, "Oscillatory shear of suspensions of noncolloidal particles," Journal of Rheology (1978-present) **50**, 711–728 (2006).
[36] Hyun-Ok Park, Jonathan M Bricker, Michael J Roy, and Jason E Butler, "Rheology of oscillating suspensions of noncolloidal spheres at small and large accumulated strains," Physics of Fluids **23**, 013302 (2011).
[37] Yuan Lin, Nhan Phan-Thien, and Boo Cheong Khoo, "Short-term and long-term irreversibility in particle suspensions undergoing small and large amplitude oscillatory stress," Journal of Rheology **57**, 1325–1346 (2013).
[38] Laurent Corte, PM Chaikin, Jerry P Gollub, and DJ Pine, "Random organization in periodically driven systems," Nature Physics **4**, 420–424 (2008).
[39] Bloen Metzger and Jason E Butler, "Clouds of particles in a periodic shear flow," Physics of Fluids **24**, 021703 (2012).
[40] F. Blanc, E. Lemaire, and F. Peters, "Tunable fall velocity of a dense ball in oscillatory cross-sheared concentrated suspensions," Journal of Fluid Mechanics **746**, R4 (2014).
[41] Jason E Butler, "Suspension dynamics: moving beyond steady," Journal of Fluid Mechanics **752**, 1–4 (2014).
[42] M. R. Maxey and B. K. Patel, "Localized force representations for particles sedimenting in stokes flow," International Journal of Multiphase Flow **27**, 1603–1626 (2001).
[43] E Climent and M.R Maxey, "Numerical simulations of random suspensions at finite reynolds numbers," International Journal of Multiphase Flow **29**, 579 – 601 (2003).
[44] E. Climent and M. R. Maxey, "The force coupling method: a flexible approach for the simulation of particulate flows," (Transworld Research Network, 2009) Chap. 7, pp. 1–21.
[45] K. Yeo and M. R. Maxey, "Dynamics of concentrated suspensions of non-colloidal particles in couette flow," Journal of Fluid Mechanics **649**, 205–231 (2010).
[46] K. Yeo and M. R. Maxey, "Simulation of concentrated suspensions using the force-coupling method," Journal of Computational Physics **229**, 2401–2421 (2010).
[47] K. Yeo, *Some aspects of suspension flows: Stokes to turbulent flows*, Ph.D. thesis, Brown University (2011).
[48] L. Durlofsky, J. F. Brady, and G. Bossis, "Dynamic simulation of hydrodynamically interacting particles," Journal of Fluid Mechanics **180**, 21–49 (1987).
[49] S. Gallier, E. Lemaire, L. Lobry, and F. Peters, "A fictitious domain approach for the simulation of dense suspensions," Journal of Computational Physics **256**, 367–387 (2014).
[50] K. L. Johnson, *Contact Mechanics* (Cambridge University Press, 1987).
[51] Margarida Machado, Pedro Moreira, Paulo Flores, and Hamid M Lankarani, "Compliant contact force models in multibody dynamics: Evolution of the hertz contact theory," Mechanism and Machine Theory **53**, 99–121 (2012).
[52] A. Nir and A. Acrivos, "On the creeping motion of two arbitrary-sized touching spheres in a linear shear field," Journal of Fluid Mechanics **59**, 209–223 (1973).
[53] J. Schäfer, S. Dippel, and D. E. Wolf, "Force schemes in simulations of granular materials," Journal de Physique I **6**, 5–20 (1996).
[54] L. Silbert, D. Ertas, G. S. Grest, T. C. Halsey, D. Levine, and S. J. Plimpton, "Granular flow down an inclined plane: Bagnold scaling and rheology," Physical Review E **64**, 051302 (2001).
[55] G. K. Batchelor, "The stress system in a suspension of force-free particles," Journal of Fluid Mechanics **41**, 545–570 (1970).
[56] Samuel H Maron and Percy E Pierce, "Application of ree-eyring generalized flow theory to suspensions of spherical particles," Journal of Colloid Science **11**, 80–95 (1956).
[57] F. Boyer, É. Guazzelli, and O. Pouliquen, "Unifying suspension and granular rheology," Physical Review Letters **107**, 188301 (2011).
[58] Neil YC Lin, Ben M Guy, Michiel Hermes, Chris Ness, Jin Sun, Wilson CK Poon, and Itai Cohen, "Hydrodynamic and contact contributions to continuous shear thickening in colloidal suspensions," Physical Review Letters **115**, 228304 (2015).
[59] Sangtae Kim and Seppo J Karrila, *Microhydrodynamics: principles and selected applications* (Heinemann, Boston,

1991).
[60] Adolfo J Banchio and John F Brady, "Accelerated stokesian dynamics: Brownian motion," The Journal of chemical physics **118**, 10323–10332 (2003).